

Sanxicun Landslide: An Investigation of Progressive Failure of a Gentle Bedding Slope

Xiangjun Pei

Chengdu University of Technology

Shenghua Cui (✉ shenghuacui.geo@gmail.com)

state key laboratory of Geohazard Prevention and Geoenvironment protection <https://orcid.org/0000-0002-6638-230X>

Ling Zhu

Chengdu University of Technology

Hui Wang

Chengdu University of Technology

Luguang Luo

Chengdu University of Technology

Xiaochao Zhang

Chengdu University of Technology

Research Article

Keywords: Gentle bedding slope, depression belt, historical earthquakes, rainfall water, progressive failure

Posted Date: May 26th, 2021

DOI: <https://doi.org/10.21203/rs.3.rs-524675/v1>

License:  This work is licensed under a Creative Commons Attribution 4.0 International License.

[Read Full License](#)

Version of Record: A version of this preprint was published at Natural Hazards on September 25th, 2021.
See the published version at <https://doi.org/10.1007/s11069-021-05044-6>.

Sanxicun landslide: an investigation of progressive failure of a gentle bedding slope

Xiangjun Pei¹; Shenghua Cui^{1,2}; Ling Zhu^{1,3}; Hui Wang¹; Luguang Luo^{1,4}; Xiaochao Zhang¹

¹ State Key Laboratory of Geohazard Prevention and Geoenvironment Protection, Chengdu University of Technology, Chengdu 610059, China.

² Disaster Prevention Research Institute, Kyoto University, Uji, 6110011, Kyoto, Japan.

³ Priority Research Center for Geotechnical Science and Engineering, The University of Newcastle, Callaghan, NSW 2308, Australia.

⁴ University of Twente, Faculty of Geo-Information Science and Earth Observation (ITC), PO Box 217, Enschede, AE 7500, Netherlands

Abstract: A gentle bedding slope (16° dip angle) failure at Sanxicun (SXC) village in Dujiangyan city was triggered by heavy rainfall in 2013. The landslide (composing of sandstone and mudstone strata) has a sliding distance of up to 1200 m and caused 166 deaths. After this failure event, a detailed field survey and a series of laboratory tests were carried out by us to investigate the progressive failure mechanism of the slope. The results revealed that the slope deformation could be traced back to the Ming Dynasty in China (400 years before) at least. A sliding block with a width of 330 m and a length of 240 m detached its original position, resulting in a depression belt with 10 m in width and 25 m in depth at the rear of the sliding block. On the scarp, a large number of cracks were widely observed not only in the sandstone but also in the mudstone. The field evidence revealed that the depression belt and cracked mudstone had provided convenience for water infiltration for a long time. The shake table test results showed that these cracks could be initiated and propagated in the slope during earthquakes. Especially, seismic stresses amplifications were induced in the mudstone to degrade this layer obviously. Besides, Direct shear tests of cracked mudstone with different immersion time were carried out. It was showed

22 that the shear strength of mudstone decreased rapidly in the initial immersion and then tends to be stable gradually. Finally,
23 numerical calculation indicated that the hydrostatic pressure in the depression belt and uplift pressure in the basal layer
24 generated by the strongest rainwater in history (537.4 mm daily) caused the kilometer- slide of the block in 2013. We
25 concluded that the catastrophic failure of the SXC landslide triggered by the rainwater in 2013 strongly depended on the
26 pre- existing deformation and damage caused by historical earthquakes and rainwaters.

27 **Keywords:** Gentle bedding slope; depression belt; historical earthquakes; rainfall water; progressive failure

28 1. Introduction

29 From 8:00 on July 8 to 8:00 on July 10, 2013, there was a continuous heavy rainfall process in Dujiangyan city, with
30 cumulative precipitation of 537.4mm. The rainfall triggered a rapid and long run-out landslide with a volume of 1.47×10^6
31 m^3 in Sanxicun (SXC) village, Dujiangyan city, Sichuan Province. The SXC landslide was located at $E103^{\circ}33'48''$,
32 $N30^{\circ}54'55''$, and 68 km away from Chengdu city. The total volume of the source area was $1.77 \times 10^6 m^3$. The whole landslide
33 mass moved downward about 50 to 80 m. The volume of the residual sliding mass was approximately $1.47 \times 10^6 m^3$. A
34 sliding mass with a volume of about $300 \times 10^3 m^3$ was initiated at a high-level position, resulting in 166 deaths. The landslide
35 was located southwest and 12 km away from the epicenter of the 2008 Wenchuan Ms 8.0 earthquake. Strong seismic
36 shaking in the landslide area induced seismic intensity of IX degree. Besides the SXC landslide, there were three small-
37 scale landslides triggered by the Wenchuan earthquake (Yin et al., 2016). There was a depression belt with a depth of 25
38 m and a maximum width of 10 m at the rear edge on the slope before the SXC landslide, suggesting it's an old landslide.
39 According to historical records, the depression belt was formed 400 years ago (Li 1998).

40 The initiation and movement mechanisms of the SXC landslides have attracted much attention from researchers. Du et
41 al. (2016) estimated that the SXC landslide had been in the critical state to sliding when the water head height of the
42 depression belt reached 9.8 m. Yin et al. (2016) argued that not only hydrostatic pressure but also uplift pressure induced
43 the failure which was assumed as four stages, i.e., cracking, creeping, separating, and residual accumulating. Wu et al.

44 (2017) proposed a model to consider the hydrostatic pressure along the bedding plane that could effectively estimate the
45 stability of the landslide. Although the formation of the landslide can be summarized as a “translational landslide induced
46 by heavy rainfall” and the landslide should be returned to stability after high water pressures were relieved (Chen and Cui,
47 2017). Luo et al. (2018) suggested that the failure process of the SXC landslide should be simulated by a thermo- poroelastic
48 approach coupled with the Savage-Hutter model. The 2008 Wenchuan earthquake was considered as a factor for the pre-
49 failure of the 2013 landslide event by Gao et al. (2017).

50 It was indisputable that the heavy rainfall event in 2013 (which was the most severe successively in history) triggered
51 the landslide. Beyond the rainfall, it was generally believed that the historical earthquakes and long- term gravity were
52 important contributors to this progress landslide (Gao et al., 2017). It was recognized that not only a large number of
53 coseismic landslides were triggered, but seismic cracks and accelerated deformation in slope were also induced during a
54 strong earthquake (Cui et al., 2012, 2014; Fu et al., 2020). These cracks in slopes provided paths for preferential flow,
55 which was associated with rainfall- induced landslide initiation (Krzeminska et al., 2013 and Shao et al., 2015). Cumulative
56 damage and progressive deformation induced by preparatory factors over time could destabilize a relatively stable rock
57 slope by initiating and propagating new cracks. Thus, the initiation of catastrophic failure of slope caused by a certain
58 earthquake or rainwater strongly depends on pre- existing damage (Gischig et al., 2016).

59 The SXC landslide is one with progressive failure as long as several hundred years. However, the study of the seismic-
60 dependent progressive failure of this landslide in the earthquake- prone area and its contribution to the 2013 landslide even
61 is limited. In this study, a detailed field investigation and a series of laboratory tests were carried out for the landslide. We
62 aimed to show the earthquake- induced pre- failure of the landslide and the role of pre- existing damage in landslide
63 initiation.

64 **2. Geological and meteorological conditions**

65 The study area is located in the transition zone between Chengdu Plain and Longmenshan tectonic belt (Fig. 1) where
66 the terrain was characterized by middle- low mountain and tectonic erosion landforms. The topographic elevation of the
67 study area is in the range from 2500 m asl in the northwest to 730 m asl in the southeast. The Longmenshan fault zone is
68 composed of the Wenchuan-Maowen fault, Yingxiu-Beichuan fault, and Pengzhou-Guanxian fault. Among these faults,
69 the Yingxiu- Beichuan fault with a strike of NE-SW and a dip of 300° to 330° and Pengzhou-Guanxian fault with a strike
70 of NE-SW and a dip of 310° to 330° were both ruptured during the 2008 Wenchuan earthquake, and the Pengzhou-
71 Guanxian fault is only 3 km away from the study landslide. The LMS belt can be divided into three main
72 tectonostratigraphic units, i.e., a Mesoproterozoic basement, pre-Indosinian marine sediments from the Sinian to the
73 middle-upper Triassic, and Indosinian terrestrial sediments (Cui et al. 2020). The study area is a part of the Qingcheng-
74 Qingxia Neocathaysian structure system, which is mainly composed of a series of NNE- trending folds, faults and
75 Quaternary depressions. The strata in this area is mainly composed of fluvial facies conglomerate, sandstone, siltstone and
76 mudstone of Jurassic, Cretaceous and Paleogene. Li et al. (2017) reported that the intense earthquake events were induced
77 by the NE-SW fault system. According to statistics, 197 earthquakes with $M_s > 4.7$ have occurred along the belt, including
78 three earthquakes with $M_s > 8.0$.

79 The study area is abundance of precipitation and rainstorm. The annual average precipitation was 1131.3 mm, and the
80 maximum annual precipitation was 1605.4 mm in 1978. By analyzing the precipitation data from 1987 to 2012, it can be
81 found that up to 77.1% of precipitation was concentrated on the rainy season, i.e., from May to September. Particularly
82 from July to August, when the 2013 landslide event occurred, the precipitation reached 490.9 mm, accounting for 45.9%
83 of the annual precipitation (Fig. 2a). The maximum monthly precipitation was 592.9 mm generated on August 1981, and
84 the maximum single-day precipitation was 213.4 mm, also generated in June 1980, both around the time when the 2013
85 landslide occurred. On July 10, 2013, the study area was suffered the largest precipitation on records. The accumulated

86 precipitation of 920 mm from 8:00 am on July 8 to 8:00 am (Fig. 2b).

87 3. Method

88 Field investigation was performed using Google Earth images, an unmanned aerial vehicle (UAV), 1:200,000- scale
89 geological maps, a laser rangefinder and compasses. Using the Google Earth images and UAV, we were able to determine
90 the overall topography and landform characteristics of the SXC landslide and its surrounding area. A digital elevation
91 model (DEM) with a resolution of 0.2 m was obtained. The 1: 200,000- scale geological maps were employed to determine
92 the geological conditions in the study area. The laser rangefinder and compass were used to determine the spatial
93 distributions, orientations, and sizes of some tension cracks.

94 Field investigation results revealed that the lithology of the landslide area was mainly composed of red thick sandstone
95 interbedded with thin mudstone. To investigate the dynamic response characteristics of this kind of slope during earthquake,
96 a shaking table test was carried out by simplified the slope into a block model. By using the shaking table tests the dynamic
97 behavior of the sandstone (hard layer) interbedded with mudstone (weak layer) in the SXC landslide could be estimated to
98 show the effect of historical earthquake on the slope deformation. To investigate the influence of water on the shear strength
99 properties of mudstone, the direct shear test for samples with different initial water contents and different immersion times
100 were carried out. Finally, on the basis of considering cumulative damage induced by historical earthquakes and mudstone
101 softening, the factor of stability (F_s) of SXC gentle bedding slope in the natural state, only sliding surface in the saturated
102 zone and different water head heights was calculated.

103 4. Results

104 4.1 SXC landslide characteristics

105 The landslide in 2013 involved a volume of $177 \times 10^4 \text{ m}^3$ with a maximum length of 1.18 km and an average width of 150
106 m. The elevations of the failure block range between 740 and 1132 m, and the topographic slope gradients range from 12°

107 to 24°. According to the remote sensing images, it can be found that the north and west sides of the landslide area are steep
108 cliffs before and after the landslide (Fig. 3), and a seasonal gully with a strike of S- N is developed on the east side of the
109 slope. The landslide area can be divided into three zones: source area (I), ploughing area (II) and accumulation area (III)
110 (Fig. 4a). The strata of the block in the source area is mainly composed of thick sandstone interbedded with thin mudstone
111 within the Guankou Formation of the Cretaceous system (K₂g) (Fig. 4b). A volume of approximately 300×10³ m³ was
112 detached from the source area. The ploughing area with an average slope angle of 27° is distributed at elevations from 850
113 to 1050 m, and the height difference is 200 m. The sliding mass continuously collides and disintegrates in the ploughing
114 area to form debris flow in the process of movement. The debris moved downslope in two directions, subsequent forming
115 a major slide area (III₁). A branch slide area is also can be found at the west part of the slope (III₂). III₁ subjected to direction
116 turning from the front valley, the debris flowed directly impacted the valley's right side after moving about 80 m resulting
117 in 166 deaths (Yin et al., 2016). The debris on the slope is mainly composed of rock blocks, shoveled soil and trees, and
118 the maximum diameter of the rock block is up to 5 m (Yin et al., 2016).

119 Although the residual sliding mass retained a relatively complete rock mass structure, several obvious tension cracks in
120 the residual sliding mass were developed (Fig. 5a and b). Details of these tension cracks are listed in Table. 1. A depression
121 belt with a strike of NE-SW, a depth of 30 m, a width of 64 m and a length of 250 m (Fig. 5c), which was formed by the
122 propagating and stretching during the 2013 landslide event based on a previous depression belt with a width of 10 m, a
123 depth of 25 m. The previous depression belt was formed 400 years ago.

124 The orientation of the bedding plane is N13°W/NE/16° (strike/dip/dip angle), showing a typical gentle rock bed. Two
125 sets of joints were developed in this area. J1 shows an orientation of N 63° W/NE/87° and is in accordance with the
126 orientation of the most tension cracks on the slope, including the depression belt (Fig. 6). J2 shows an orientation of S 39°
127 W/NW/82°. Fig. 7 shows that solution traces induced by the water flow have appeared on the landslide scarp. A layer of
128 calcareous film with a thickness of 0.3-0.5 cm was found. In addition, it should be noted that the mudstone on the basal

129 layer of the residual block is highly fragmented (Fig. 8a). According to the characteristics of crack propagation in mudstone
130 layer, it can be divided into three types of cracks: gently inclined cracks with dip angle below 30° , moderately -gently
131 inclined cracks with dip angle $30^\circ - 60^\circ$, and steeply inclined cracks with dip angle above 60° . According to the
132 statistical results of cracks in the mudstone layer, the proportion of each type of cracks is shown in Fig. 8b. From Fig. 8b,
133 the gently inclined cracks are the most, accounting for about 47%, while the steeply inclined cracks are the least, accounting
134 for about 21%. In addition, salt was extracted from the fragmented mudstone. These suggested that long- term groundwater
135 activity had been in the slope, especially on interfaces and in cracks of the mudstone on the landside's basal sliding layer
136 (Fig. 8c).

137 4.2 Experimental data

138 4.2.1 Shaking table test

139 A simplified model with bedding strata, sliding surface and slide block for the SXC landslide are shown in Fig. 9.
140 Historical seismic wave propagated to SXC slope and produced horizontal and vertical ground motion in the inclined weak
141 layer. The vertical seismic force can be decomposed into normal and tangential force components (Fig. 10a), and SN and
142 EW horizontal seismic forces can be decomposed into normal and tangential force components (Fig. 10b). To reduced the
143 topography- depended influence on the dynamic responding of model, the inclined weak layer is rotated to horizontal, the
144 seismic stress in the weak layer will be simplified into two components: vertical and horizontal (Fig. 10c). Then, the model
145 shown in Fig. 11a is recommended in our shaking table test. The acceleration, soil pressure and displacement sensors were
146 used. The soil pressure and acceleration sensors were arranged in the upper (hard) layer, weak layer and lower (hard) layer.
147 The upper and lower layer represented the sandstone strata and the middle layer represented the mudstone strata. The
148 displacement sensors were respectively installed in the upper and lower hard layers near the interfaces of the weak layer.
149 The scheme is shown in Fig. 11b.

150 The similitude laws are basic theories that ensure that model experimental results are similar to those of a prototype. It
151 is important to correctly scale down the parameters of the model experiment based on the similitude laws and select the
152 right materials. In this paper, the elastic modulus of the mudstone layer was assumed as the most different property from
153 the lower and upper sandstone layers. Thus, for the tests, this factor was represented as closely as possible because it should
154 have a significant influence on the response of the model. Moreover, the density (ρ), length (L), gravity (g), seismic
155 frequency (f), and time (t) were also considered. [Table. 2](#) presents the scaling factors for this study. Based on these
156 similitude laws, the parameters of the experimental model were set, and suitable materials were selected.

157 According to a series of physical and mechanical tests, the materials of the middle layer were mainly formed of quartz
158 sand, clay, liquid paraffin, and plaster at ratios of 17: 80: 2: 1, and they were mixed with 17.02 % of water. The materials
159 in the upper and lower layer of the model were formed of barite: quartz sand: plaster: iron slag at ratios of 37.5: 37.5: 7:18,
160 and they were mixed with 11.5 % of water and 2.3 % of glycerol. The parameters of the similar material were listed in
161 [Table. 3](#).

162 Due to that, the tests were used to investigate the possible influences of the earthquake on the slope, not to reproduce the
163 landslide process. Sine wave was applied in our tests, according to the Wenchuan earthquake recorded at the MZQ051
164 seismic station 103 km away from the landslide. The duration on the record from 37 to 55 s was the main shaking part, in
165 which the peak acceleration was 0.84 g and the frequency was in the range of 1-10 Hz. The waveform of the input shaking
166 was a sinusoidal curve with a duration of 15 s, a maximum acceleration of 0.8 g and a maximum frequency of 15 Hz.

167 The typical results of the shaking table test under the condition of a sine wave with 0.3 g acceleration and 15 Hz frequency
168 are shown in [Fig. 12](#). From [Fig. 12a](#) and [12b](#), the peak accelerations in the upper hard layer, weak layer and lower hard
169 layer under vertical vibration are approximately equal, about 0.31 g. However, during horizontal vibration, the peak
170 acceleration gradually increases with the height of the model. The peak accelerations in the lower hard layer, weak layer

171 and upper hard layer are 0.31 g, 0.39 g and 0.44 g, respectively. The elevation amplification effect of acceleration is obvious.
172 From Fig. 12c and 12d, the peak displacements in the lower hard layer and the upper hard layer under vertical vibration
173 are 0.022 mm and 0.114 mm, respectively, and the displacement difference is 0.09 mm. The peak displacements in the
174 lower hard layer and the upper hard layer under horizontal vibration are 0.021 mm and 0.067 mm, respectively, and the
175 displacement difference is 0.046 mm. It is revealed that the peak displacements in the upper hard layer are obviously greater
176 than that of the lower hard layer in both horizontal and vertical vibrations. Besides, an interesting note is that the
177 displacement response time of the upper hard layer is significantly delayed compared to the lower hard layer. From Fig.
178 12e and 12f, the soil pressure in the weak layer under vertical vibration is 0.65 kPa, and the soil pressures in the upper and
179 lower hard layers are approximately equal, about 0.056 kPa. Besides, the soil pressure in the weak layer under horizontal
180 vibration is 1.14 kPa, and the soil pressures in the upper and lower hard layers are only 0.1 kPa. The calculation showed
181 that the weak layer's soil pressures are 11.6 and 11.4 times these of the upper and lower layers, respectively.

182 The seismic wave propagates in different rock layers of the test model, the discontinuous medium (hard layer and weak
183 layer) causes to reflection and refraction of the seismic wave at the interface. Primarily when the seismic wave propagates
184 from hard rock to soft rock, incompatible deformation is generated as shown by our data due to hard layer and weak layer
185 with significant differences in strength, elastic modulus and deformability (Pei et al., 2018). We found that the incompatible
186 deformation caused two kinds of dynamic effects on the weak layer. Under the condition of vertical vibration, the
187 displacement amplitudes in upper and lower hard layers are obviously different. In the process of downward movement of
188 the shaking table, large displacement in the upper hard layer and small displacement in the lower hard layer caused
189 amplified compression stress in the weak layer. Similarly, the amplified tension stress was generated in the weak layer in
190 the upward movement (Fig. 13a). Besides, in the process of horizontal movement, the large displacement of the upper hard
191 layer and the small displacement of the lower hard layer inevitably led to the dislocation between the upper and lower hard
192 layers, and then amplified shear stress was generated in the weak layer (Fig. 13b).

193 4.2.2 Direct shear test data

194 The direct shear test results for samples with different water contents (w) are shown in Fig. 14. It is clear that no obvious
195 peak point in the stress- displacement curves of the sample appeared under $\sigma= 200$ kPa (Fig. 14a), showing hardening
196 characteristic. According to the Trade Standard of P. R. China SL237-021 (1999), the shear stress corresponding to the
197 shear displacement 4 mm is selected as the shear strength. From Fig. 14b, the shear strength increases firstly and then
198 decreases with raising water content. The maximum shear strength is obtained when the water content is 9 %. From Fig.
199 14c, the internal friction angle and cohesion increase from 18.61° and 54.8 kPa ($w= 6\%$) to 21.7° and 78.66 kPa ($w= 9\%$),
200 respectively. Afterward, the internal friction angle and cohesion decrease with the increment of water content. When the
201 water content is 18%, the internal friction angle and cohesion are only 17.68° and 15.24 kPa. Table. 4 shows the change
202 rate of the shear strength parameters of the samples with increasing water content. The cohesion decreases obviously with
203 increasing water content, while the influence of water content on internal friction angle is relatively small. The change
204 ratios of internal friction angle and cohesion are -28.17% and -72.2%, respectively.

205 The direct shear test results for samples with different immersion times (t) are shown in Fig. 15. From Fig. 15a, the
206 shear stress- displacement curves under $\sigma= 200$ kPa tend to harden without an obvious peak point. From Fig. 15b, the shear
207 strengths decrease with the increment of immersion time. During the first hour of immersing the samples, the shear strength
208 reduces rapidly and then tends to be stable with increasing immersion time. From Fig. 15c, the internal friction angle and
209 cohesion decrease from 22.24° and 50.91 kPa to 16.79° and 15.22 kPa in the first hour, respectively. Then, the cohesion
210 remains stable. However, the internal friction angle increases to 19.81° (immersion for 24 h) and decreases to 16.38°
211 (immersion for 96 h). Table. 5 shows the change rate of shear strength parameters with increasing immersion time. After
212 immersion for 96 h, the change rates of internal friction angle and cohesion are -41.98% and -79.8%, respectively, which
213 mainly occurs in the first hour.

214 Our tests indicate that the immersion time has a more significant influence on the attenuation of cohesion. Zhang et
 215 al. (2016) reported that water would enter the poles between the particles and gradually undermined the cohesiveness under
 216 immersion conditions. Gradually, uneven inner-stress and many micropores in the mudstone would cause softening and
 217 degradation. The absorbed suction could resist the sliding of particles, and it increased with increasing water content.
 218 However, when the water content increased to a certain value, the pores were gradually filled with water and the area of
 219 capillary water decreased, resulting in a gradual decrease in the absorbed suction until it disappeared. Also, the water
 220 molecules in the red mudstone firstly cemented with free iron oxide to form a granular structure when the water content
 221 was low, resulting in a temporary increase in the internal friction angle of the mudstone.

222 4.3 Initiation model for SXC landslide

223 The water pressure that affects cracked slope stability includes hydrostatic pressure along the depression belt, uplift
 224 pressure along the sliding surface and drag force. The water level in the depression belt of the bedding slope and the uplift
 225 pressure on the sliding surface change dynamically during rainfall. If the permeability coefficient of the sliding surface is
 226 low, it will take a long time for groundwater to flow from the rear tensile crack to the shear openings at the foot of the
 227 landslide (Wu et al., 2017). The effect of water on the tension crack and sliding surface is neglected, then the calculation
 228 formula of the safety factor of profile B-B' is given by (Fig. 16):

$$229 \quad F_s = \frac{W \cos \theta \tan \varphi + cL}{W \sin \theta} \quad (1)$$

230 where F_s is the safety factor, W is the weight of the landslide profile B- B', θ is the dip angle of the slip surface, φ is the
 231 internal friction angle of the sliding surface, c is the cohesion of the sliding surface, L is the length of the sliding surface
 232 along the sliding direction.

233 The safety factor considering the effect of water pressure is obtained by:

$$234 \quad F_s = \frac{(W \cos \theta - V \sin \theta - U) \tan \varphi + cL}{W \sin \theta + V \cos \theta + T} \quad (2)$$

235 where V is the hydrostatic pressure along the depression belt, U is the uplift pressure along the sliding surface, and T is the

236 drag force.

237 The weight of the landslide profile B- B' is obtained by:

$$238 \quad W = \gamma A \quad (3)$$

239 The hydrostatic pressure can be expressed as:

$$240 \quad V = \frac{1}{2} \gamma_w H_w^2 \quad (4)$$

241 The uplift pressure is given by:

$$242 \quad U = \frac{1}{2} \gamma_w H_w L \quad (5)$$

243 The drag force can be written as:

$$244 \quad T = \gamma_w H_w b \quad (6)$$

245 where γ is the unit weight of landslide mass; A is the area of the calculation profile; γ_w is the unit weight of water; H_w is the
246 height of water level in the depression belt; b is the width of the structural plane. So, Eq. (1) can be replaced by:

$$247 \quad F_s = \frac{[2\gamma A \cos \theta - \gamma_w H_w^2 \sin \theta - \gamma_w H_w L] \tan \varphi + 2cL}{2\gamma A \sin \theta + \gamma_w H_w^2 \cos \theta + 2\gamma_w H_w b} \quad (7)$$

248 The results of the direct shear test were used to obtain F_s . The mudstone used in the direct shear test was the undisturbed
249 sample obtained from the SXC landslide, which has experienced historical earthquakes. The combined effect of historical
250 earthquakes and water on mudstone is considered in the direct shear test. Therefore, it is appropriate to use the shear
251 strength parameters obtained from the direct shear test to calculate F_s . Considering that the sliding surface was immersed
252 in water for a long time, the shear strength parameter of the sample immersed in water for 96 h was employed. The specific
253 parameter values are shown in [Table. 6](#).

254 The calculating results of F_s with various depths of groundwater are shown in [Table. 7](#). The results show that the F_s in
255 natural state is 1.59. The SXC landslide may be initiated if groundwater depth to the sliding surface exceeds 10 m.

256 **5. Discussion**

257 **5.1 Formation of the depression belt**

258 A large number of field monitoring shows amplification of peak ground acceleration (PGA) and it increases with the
259 rising elevation (Wang et al., 2010; Luo et al., 2020). The SXC landslide is located on the Longmenshan tectonic belt and
260 belongs to the Qingcheng- Qingxia Neocathaysian structure system, which is mainly composed of a series of NNE- trending
261 folds, faults and Quaternary depressions. As stated in the second section, the Longmenshan area is earthquake- prone owing
262 to the effect of the tectonic activity. In Fig. 17, we show the earthquakes with a magnitude greater than 3.0 occurred in the
263 adjacent area (within 200 km) since 1900. The number is up to 1921, which should have induced significant damage to the
264 rock mass continually in the study area due to amplification of peak ground acceleration.

265 The influence of earthquake on the slope was firstly testified by the old tension cracks observed in the upper part of the
266 slope in the landslide area, although these cracks also could be generated due to other environmental factors. Secondly, the
267 landslide scarp also involved earthquake cause. The significant difference between earthquake and gravity- induced
268 landslides was that earthquake-induced landslides generally presented steep scarp. e.g., the Daguangbao and Wenjiagou
269 landslides triggered by the 2008 Wenchuan earthquake have steep scarps with a height difference of 700 m and 445 m,
270 respectively (Deng et al., 2017; Cui et al., 2020). Generally, an arc-shaped shear failure was presented in slope deformation
271 caused by gravity (Bouissou et al., 2012). However, strong horizontal seismic force has more serious influence on slope
272 deformation, and a steep release surface in slope was usually induced by tension deformation. The horizontal earthquake
273 shaking provided seismic force in the horizontal along the landslide sliding direction. The steep- release surfaces in the
274 SXC landslide shows obvious differences in geometry from that of general gravity- induced landslides. Thus, the steep-
275 release surface in the SXC landslide can be reasonably attributed to horizontal shaking- induced tension failures, although
276 this failure is not finished in one earthquake but through fracture accumulation in history.

277 The depression belt of the SXC landslide has an important contribution to the initiation of the landslide in 2013. Based

278 on the field investigation results, we infer the formation and evolution of the tension crack before the 2013 landslide event.
279 Firstly, it is noted that the joint sets provide geological conditions for the initiation, propagation and coalescence of seismic
280 cracks. The field investigation results revealed that the orientation of J1 was in accordance with the most tension cracks.
281 The steep joint parallel to the ridge makes it easy for the rock mass to trigger tension cracks under seismic loading.
282 Therefore, it was considered that the seismic cracks were prone to initiate and propagate from the J1 tips under historical
283 earthquakes and gradually forming penetrating seismic cracks after multiple earthquakes. Furthermore, the depression belt
284 was continuously propagated under the combined effect of historical earthquakes, rainfall and gravity. Finally, the belt
285 reached the basal layer, i.e., the mudstone layer. A large failure event just like the landslide in 2013 should be triggered by
286 earthquake or rainfall 400 years ago. The sliding block stopped on the bedding after traveling some distance. The depression
287 belt with a width of 10 m, a depth of 25 m was formed. This process is shown in Fig. 22. Although there were no records
288 to show the other sliding event of the block before 400 years or during the 400 years, if it has, it is reasonable due to
289 historical earthquakes and rainfalls.

290 **5.2 Formation of the fractures on the basal layer**

291 The shaking table tests show that the weak layer is subjected to greater compressive and tensile stresses due to
292 incompatible deformation (Fig. 18). It can be reasonably proposed that the cyclic stress amplification caused the initiation
293 and propagation of fractures in the weak layer, which were confirmed by the a large number of cracks observed in the
294 mudstone on the sliding basal layer of the landslide (Pei et al., 2018).

295 Figs. 19 and 20 were used to shows the mechanisms of the cracks observed in the mudstone layer under compression
296 and tension stresses during the earthquake. Fig. 19 shows that compression stress will be concentrated at the tip of the
297 original joint in the rock mass. If the compression stress exceeds the strength threshold of the joint tip, the compression
298 crack will be initiated and propagated at the end of the joint. Further, the stress concentration position will be transferred
299 to the interior of the rock mass. The resilience of the crack tip is weakened in the unloading process, but the elastic modulus

300 of rock is much higher, resulting in the differential rebound, which will produce residual tension stress and compression
301 stress at the interface between the rock and the crack, causing the crack to propagate to both ends.

302 [Fig. 20a](#) shows mechanisms of crack propagation under tension stress. Under the condition of tension stress, the tension
303 stress at both tips of the joint is concentrated. When it is greater than the tensile strength of the rock mass, seismic cracks
304 nearly parallel to the tensile stress are formed, and almost horizontal and gently inclined cracks are formed. Because the
305 tension strength of rock mass is far less than the compression strength, the above-mentioned tension cracks are very easy
306 to occur. In addition, under the condition of compression stress, the most concentrated tension stress is located at the end
307 of the crack with the angle of 30° - 40° with the direction of the principal compression stress. Therefore, the fracture first
308 appears at the end of some joints with favorable orientation and then develops into secondary cracks (J_{2t}). The angle
309 between the crack propagation direction and the long axis direction of the joint is about 2β , and then gradually turns parallel
310 to the direction of the maximum principal the most concentrated tension stress is located at the end of the crack with an
311 angle of 30° - 40° with the direction of the principal compression stress, resulting in nearly vertical cracks with high dip
312 angle ([Fig. 20b](#)). Under the condition of cyclic shear stress, tension and compression - torsion en- echelon cracks are
313 developed. The propagation direction of tension en- echelon cracks (T) is generally parallel to the maximum principal
314 compressive stress, and sometimes two groups of conjugate secondary shear cracks (R, R') can be formed. In addition, the
315 developed direction of compressive- torsion cracks (P) intersects with the shear direction at an acute angle ([Fig. 21](#)).

316 **5.3 Progressive failure of SXC landslide**

317 Earthquakes have been recognized as an important factor triggering the catastrophic failure of large-scale landslides.
318 However, seismic waves are not just a trigger mechanism. They also lead to progressive failure on rock slopes, which is a
319 very effective fatigue process in deformation and damage of rock slopes ([Gischig et al., 2016](#)). Such as the progressive
320 failure of SXC landslide in at least 400 years, which is affected by joints, historical earthquakes, rainfall, gravity and other
321 factors.

322 The 2008 Wenchuan earthquake has attracted considerable attention because it triggered more than 60,000 landslides in
323 an elliptical area along with the fault ruptures (Dai et al., 2011; Gorum et al., 2011). However, the earthquake has been
324 given little attention in contributing to the progressive damage and the incremental destabilization of rock slopes.
325 Considering that this study area is located in the eastern margin of the Qinghai Tibet Plateau, a lot of active fault zones are
326 distributed in the region due to the Indian plate squeezing the Eurasian plate (e.g., Longmenshan fault zone, Xianshuihe
327 fault zone, Anninghe fault zone and Xiaojiang fault zone, etc.). In history, several disastrous earthquakes occurred in these
328 active faults, including the 1786 Ms 7.8 Kangding earthquake (Petley 2008), 1933 Diexi Ms 7.5 earthquake (Ren et al.,
329 2018) and 2008 Wenchuan Ms 8.0 earthquake (Huang and Fan 2013). These induced the damage accumulation in slopes
330 in this region.

331 Similarly, rainfall plays the same role, and the hydrostatic pressure and softening on sliding surfaces induced by repeated
332 rainfall might cause instantaneous deformation of slope. Our shaking table tests, immersion tests and direct shear tests
333 simulate one earthquake, one rainfall, or one shear failure. Their results should be coupled and accumulated, which should
334 be further study. In this study, the rainstorm in 2013 accelerated the slope deformation to reach the critical state, resulting
335 in the landslide initiation. It can be inferred that the catastrophic failure of the SXC landslide triggered by the rainfall in
336 2013 strongly depends on the pre- existing deformation and damage caused by historical earthquakes, rains and gravity
337 (Fig. 23).

338 The progressive deformation and failure of slope are the results of the integrated influence of several factors, which
339 includes geological structure, preparatory factors and triggering factors (Fig. 24) (Gunzburger et al., 2005). The SXC
340 landslide with a failure history of more than 400 years is a typical example for progressive failure study. Based on our
341 understanding of its history, we made Fig. 24 to illustrate the possible effect factor of the landslide from stability to be
342 instability.

343 The rock mass structure is mainly composed of the primary structure determined by the rock formation environment and
344 secondary structure caused by tectonic activity after diagenesis. Some common primary structures include contact surface,
345 flow layer and primary joint in magmatic rock, bedding plane, foliation and weak rock in sedimentary rock, and schistosity
346 and gneissic in metamorphic rock. Typical secondary structures include joint, fault fracture zone and bedding fault zone.
347 The presence of these structures provides convenience for the initiation and propagation of shear and tension cracks under
348 endogenic and exogenic processes, which is the geological basis for the formation of landslide boundaries (Liu et al., 2018;
349 Song et al., 2018).

350 Over a long period of time (e.g., 10-100,000 years), different types of preparatory factors gradually reduce the rock mass
351 strength and slope resistance. The fatigue process has been discussed; e.g., water pressure changes induced by rainfall,
352 snowmelt or reservoir level (Bonzanigo et al., 2007; Zangerl et al., 2010), thermal stress changes (Gischig et al., 2011;
353 Grämiger et al., 2018), seismic stress (Gischig et al., 2016), glacial loading and unloading (Leith et al., 2014) and long-
354 term weathering (Jaboyedoff et al., 2004; Li et al., 2018), etc. These preparation factors can also be regarded as triggering
355 factors to trigger slope failure. The triggering factors are the change of driving force acting on the slope in a short period
356 (e.g., several seconds to several years), which eventually causes catastrophic failure of the slope. Triggering factors are
357 usually reported to be the cause of slope failure. It is noted that these factors can affect slope stability simultaneously and
358 jointly. For example, repeated seismic loading may cause significant incremental damage in the form of crack initiation
359 and propagation, which causes the rock mass to reach a highly critical state (Moore et al., 2012). On this basis, a small
360 disturbance- an earthquake or water pressure induced by rainfall or snowmelt- may cause the catastrophic failure of the
361 slope, and even the increase of pressure during the ordinary seasonal cycle may trigger the slope failure if the slope is in a
362 sufficiently critical state. As a whole, these factors may not directly cause slope failure but can contribute to cumulative
363 damage and progressive deformation of rock slope.

364 **6. Conclusion**

365 In this study, to investigate the initiation mechanism of the cracked slope in earthquake- prone areas, a detailed field
366 investigation and a series of laboratory tests were carried out. It is revealed that a sliding block with a width of 330 m and
367 a length of 240 m detached its original position, resulting in a depression belt with 10 m in width and 25 m in depth at the
368 rear of the sliding block. The cyclic stress amplification induced by incompatible deformation caused the initiation and
369 propagation of a large number of cracks in the mudstone. The shear strength of cracked mudstone decreased rapidly in the
370 initial immersion and then tends to be stable gradually. Finally, the landslide was triggered by hydrostatic pressures induced
371 by the most significant precipitation in Dujiangyan City since meteorological records. It is proposed that the catastrophic
372 failure of the SXC landslide triggered by the rainwater in 2013 strongly depended on the pre- existing deformation and
373 damage caused by historical earthquakes and rainwaters.

374 **Acknowledgments**

375 This study was partially supported by the National Key R&D Program of China (Grants No. 2017YFC1501002) and the
376 National Natural Science Foundation of China (Grants No. 41931296, 41907254, 41521002).

377 **Declarations**

378 **Conflict of interest** The authors declare that they have no known competing financial interests or personal relationships
379 that could have appeared to influence the work reported in this paper.

380 **References**

- 381 Bonzanigo, L., Eberhardt, E., & Loew, S. (2007). Long-term investigation of a deep-seated creeping landslide in crystalline
382 rock. Part I. Geological and hydromechanical factors controlling the Campo Vallemaggia landslide. *Canadian*
383 *Geotechnical Journal*, 44(10), 1157-1180.
- 384 Bouissou, S., Darnault, R., Chemenda, A., Rolland, Y., 2012. Evolution of gravity-driven rock slope failure and associated
385 fracturing: Geological analysis and numerical modelling. *Tectonophysics* 526, 157–166.
- 386 Chen, X. Z., & Cui, Y. F. (2017). The formation of the Wulipo landslide and the resulting debris flow in Dujiangyan City,
387 China. *Journal of Mountain Science*, 14(6), 1100-1112.
- 388 Cui, P., Guo, C. X., Zhou, J. W., Hao, M. H., & Xu, F. G. (2014). The mechanisms behind shallow failures in slopes
389 comprised of landslide deposits. *Engineering geology*, 180, 34-44.

390 Cui, P., Lin, Y. M., & Chen, C. (2012). Destruction of vegetation due to geo-hazards and its environmental impacts in the
391 Wenchuan earthquake areas. *Ecological Engineering*, 44, 61-69.

392 Cui, S., Yang, Q., Pei, X., Huang, R., Guo, B., & Zhang, W. (2020). Geological and morphological study of the Daguangbao
393 landslide triggered by the Ms. 8.0 Wenchuan earthquake, China. *Geomorphology*, 370, 107394.

394 Dai, F. C., Tu, X. B., Xu, C., Gong, Q. M., & Yao, X. (2011). Rock avalanches triggered by oblique-thrusting during the
395 12 May 2008 Ms 8.0 Wenchuan earthquake, China. *Geomorphology*, 132(3-4), 300-318.

396 Deng, Q., Gong, L., Zhang, L., Yuan, R., Xue, Y., Geng, X., & Hu, S. (2017). Simulating dynamic processes and
397 hypermobility mechanisms of the Wenjiagou rock avalanche triggered by the 2008 Wenchuan earthquake using
398 discrete element modelling. *Bulletin of Engineering Geology and The Environment*, 76(3), 923-936.

399 Du, G. L., Zhang, Y. S., & Yao, X. (2016). Formation mechanism analysis of Wulipo landslide-debris flow in Dujiangyan
400 City. *Rock and Soil Mechanics*, 37(S2), 492-501. (In Chinese)

401 Fan, X., Xu, Q., Scaringi, G., Dai, L., Li, W., Dong, X., ... & Havenith, H. B. (2017). Failure mechanism and kinematics
402 of the deadly June 24th 2017 Xinmo landslide, Maoxian, Sichuan, China. *Landslides*, 14(6), 2129-2146.

403 Fu, X., Sheng, Q., Li, G., Zhang, Z., Zhou, Y., & Du, Y. (2020). Analysis of landslide stability under seismic action and
404 subsequent rainfall: a case study on the Ganjiazhai giant landslide along the Zhaotong-Qiaojia road during the 2014
405 Ludian earthquake, Yunnan, China. *Bulletin of Engineering Geology and the Environment*, 1-20.

406 Gao, Y., Yin, Y., Li, B., Feng, Z., Wang, W., Zhang, N., & Xing, A. (2017). Characteristics and numerical runout modeling
407 of the heavy rainfall-induced catastrophic landslide–debris flow at SXC, Dujiangyan, China, following the Wenchuan
408 Ms 8.0 earthquake. *Landslides*, 14(4), 1361-1374.

409 Gischig, V. S., Moore, J. R., Evans, K. F., Amann, F., & Loew, S. (2011). Thermomechanical forcing of deep rock slope
410 deformation: 1. Conceptual study of a simplified slope. *Journal of Geophysical Research: Earth Surface*, 116(F4).

411 Gischig, V., Preisig, G., & Eberhardt, E. (2016). Numerical investigation of seismically induced rock mass fatigue as a
412 mechanism contributing to the progressive failure of deep-seated landslides. *Rock Mechanics and Rock Engineering*,
413 49(6), 2457-2478.

414 Gorum, T., Fan, X., van Westen, C. J., Huang, R. Q., Xu, Q., Tang, C., & Wang, G. (2011). Distribution pattern of
415 earthquake-induced landslides triggered by the 12 May 2008 Wenchuan earthquake. *Geomorphology*, 133(3-4), 152-
416 167.

417 Grämiger, L. M., Moore, J. R., Gischig, V. S., & Loew, S. (2018). Thermomechanical stresses drive damage of Alpine
418 valley rock walls during repeat glacial cycles. *Journal of Geophysical Research: Earth Surface*, 123(10), 2620-2646.

419 Gunzburger, Y., Merrien-Soukatchoff, V., & Guglielmi, Y. (2005). Influence of daily surface temperature fluctuations on
420 rock slope stability: case study of the Rochers de Valabres slope (France). *International Journal of Rock Mechanics
421 and Mining Sciences*, 42(3), 331-349.

422 Huang, R., & Fan, X. (2013). The landslide story. *Nature Geoscience*, 6(5), 325-326.

423 Jaboyedoff, M., Baillifard, F., Bardou, E., & Girod, F. (2004). The effect of weathering on Alpine rock instability. *Quarterly
424 Journal of Engineering Geology and Hydrogeology*, 37(2), 95-103.

425 Krzeminska, D. M., Bogaard, T. A., Malet, J. P., & Van Beek, L. P. H. (2013). A model of hydrological and mechanical
426 feedbacks of preferential fissure flow in a slow-moving landslide. *Hydrology and Earth System Sciences*, 17(3), 947-
427 959.

428 Lajtai, E. Z. (1977). A mechanistic view of some aspects of jointing in rocks. *Tectonophysics*, 38(3-4), 327-338.

429 Leith, K., Moore, J. R., Amann, F., & Loew, S. (2014). Subglacial extensional fracture development and implications for
430 Alpine Valley evolution. *Journal of Geophysical Research: Earth Surface*, 119(1), 62-81.

431 Li YQ (1998) Master Zhang Daqian and Mt. Qiangcheng. *Sichuan Today* 11(4):32–34. (In Chinese)

432 Li, J., Zhou, K., Liu, W., & Zhang, Y. (2018). Analysis of the effect of freeze–thaw cycles on the degradation of mechanical
433 parameters and slope stability. *Bulletin of Engineering Geology and the Environment*, 77(2), 573-580.

- 434 Li, Y., Zhou, R.J., Yan, L., Yan, Z.K., Ding, H.R., & Shao, C.J., 2017. Active tectonics and historical earthquakes in
 435 Longmenshan. In: Feng, B. (Ed.), *Tectonic Geomorphology and Surface Process of Longmen Shan*. 56. Science Press,
 436 Beijing. (In Chinese)
- 437 Liu, X., Liu, Y., He, C., & Li, X. (2018). Dynamic stability analysis of the bedding rock slope considering the vibration
 438 deterioration effect of the structural plane. *Bulletin of Engineering Geology and the Environment*, 77(1), 87-103.
- 439 Luo, Y., Fan, X., Huang, R., Wang, Y., Yunus, A. P., & Havenith, H. B. (2020). Topographic and near-surface stratigraphic
 440 amplification of the seismic response of a mountain slope revealed by field monitoring and numerical simulations.
 441 *Engineering Geology*, 271, 105607.
- 442 Luo, Y., Liu, W., He, S., Yuanjun, J., & Lei, X. (2018). Dynamic process simulation of rainfall-induced SXC landslide
 443 based on a thermo-poro-elastic approach. *Natural Hazards*, 92(1), 415-428.
- 444 Moore, J. R., Gischig, V., Amann, F., Hunziker, M., & Burjanek, J. (2012). Earthquake-triggered rock slope failures:
 445 Damage and site effects. In *Proceedings 11th International & 2nd North American Symposium on Landslides (Vol. 1,*
 446 *pp. 869-875)*. Banff, Canada: CRC Press.
- 447 Pei, X. J., Guo, B., Cui, S. H., Wang, D. P., Xu, Q., & Li, T. T. (2018). On the initiation, movement and deposition of a
 448 large landslide in Maoxian County, China. *Journal of Mountain Science*, 15(6), 1319-1330.
- 449 Petley D (2008) The Sichuan earthquake. *Geogr Rev* 22:2-4
- 450 Ren, J., Xu, X., Zhang, S., Yeats, R. S., Chen, J., Zhu, A., & Liu, S. (2018). Surface rupture of the 1933 M 7.5 Diexi
 451 earthquake in eastern Tibet: implications for seismogenic tectonics. *Geophysical Journal International*, 212(3), 1627-
 452 1644.
- 453 Shao, W., Bogaard, T. A., Bakker, M., & Greco, R. (2015). Quantification of the influence of preferential flow on slope
 454 stability using a numerical modelling approach. *Hydrology and Earth System Sciences*, 19(5), 2197.
- 455 Song, D., Che, A., Chen, Z., & Ge, X. (2018). Seismic stability of a rock slope with discontinuities under rapid water
 456 drawdown and earthquakes in large-scale shaking table tests. *Engineering Geology*, 245, 153-168.
- 457 Song, D., Liu, X., Huang, J., Wang, E., & Zhang, J. (2021). Characteristics of wave propagation through rock mass slopes
 458 with weak structural planes and their impacts on the seismic response characteristics of slopes: A case study in the
 459 middle reaches of Jinsha River. *Bulletin of Engineering Geology and the Environment*, 80(2), 1317-1334.
- 460 Stead, D., Coggan, J. S., & Eberhardt, E. (2004). Realistic simulation of rock slope failure mechanisms: the need to
 461 incorporate principles of fracture mechanics. *International Journal of Rock Mechanics and Mining Sciences*, 41, 563-
 462 568.
- 463 Trade Standard of P.R. China, SL237-021 (1999) Standard method for direct shear test of soils. Specification of Soil Test,
 464 The Ministry of Water Resources of P. R. China, Beijing. (in Chinese)
- 465 Wang, J., Yao, L., & Hussain, A. (2010). Analysis of earthquake-triggered failure mechanisms of slopes and sliding surfaces.
 466 *Journal of Mountain Science*, 7(3), 282-290.
- 467 Wu, L. Z., Shi, J. S., & Xu, Q. (2017). The rainfall-induced Wulipo rockslide, China: a modified model for rockslide
 468 initiation. *Environmental Earth Sciences*, 76(14), 497.
- 469 Xu, Q., Liu, H., Ran, J., Li, W., & Sun, X. (2016). Field monitoring of groundwater responses to heavy rainfalls and the
 470 early warning of the Kualiangzi landslide in Sichuan Basin, southwestern China. *Landslides*, 13(6), 1555-1570.
- 471 Yin, Y., Cheng, Y., Liang, J., & Wang, W. (2016). Heavy-rainfall-induced catastrophic rockslide-debris flow at SXC,
 472 Duijiangyan, after the Wenchuan Ms 8.0 earthquake. *Landslides*, 13(1), 9-23.
- 473 Yong, R., Ye, J., Li, B., & Du, S. G. (2018). Determining the maximum sampling interval in rock joint roughness
 474 measurements using Fourier series. *International Journal of Rock Mechanics and Mining Sciences*, 101, 78-88.
- 475 Zangerl, C., Eberhardt, E., & Perzmaier, S. (2010). Kinematic behaviour and velocity characteristics of a complex deep-
 476 seated crystalline rockslide system in relation to its interaction with a dam reservoir. *Engineering Geology*, 112(1-4),
 477 53-67.

478 Zhang, S., Xu, Q., & Hu, Z. (2016). Effects of rainwater softening on red mudstone of deep-seated landslide, Southwest
479 China. *Engineering Geology*, 204, 1-13.
480

481

Table. 1 Details of these tension cracks

No	Strike (°)	Length (m)	Width (m)	Depth (m)
①	N63°W	153	\	3
②	N76°W	694	\	16
③	N49°W	350	\	10
④	N52°W	242	5	9
⑤	N28°W	106	\	6
⑥	N23°W	97	7	8
⑦	N78°W	182	3	5
⑧	N84°E	261	3	7
⑨	N73°E	108	5	6
⑩	N71°W	106	8	8
⑪	N84°W	690	\	6

482

483

Table. 2 Similarity system for shaking table test

Physical parameters	Similarity relation	Similarity coefficient	
		Sandstone	Mudstone
Density ρ	C_ρ	1*	1*
Elastic modulus E	C_E	30*	10*
Time t	C_t	10*	10*
Length l	$C_l = C_\rho^{-0.5} C_E^{0.5} C_t$	55	32
Poisson's ratio μ	C_μ	1	1
Cohesion c	$C_c = C_E$	30	10
Internal friction angle φ	C_φ	1	1
Stress σ	$C_\sigma = C_E C_\varepsilon$	54	32
Strain ε	$C_\varepsilon = C_\rho C_g C_l C_E^{-1}$	1.8	3.2
Frequency f	$C_f = C_t^{-1}$	0.1	0.1
Displacement u	$C_u = C_l C_\varepsilon$	99	102
Speed v	$C_v = C_u C_t^{-1}$	9.9	10.2
Acceleration a	$C_a = C_u C_t^{-2}$	0.01	0.01
Gravitational acceleration g	C_g	1	1

484

485

Table. 3 Physical and mechanical parameters

Material types		Density ρ (t/m ³)	Elastic modulus E (MPa)	Poisson's ratio μ	Strength σ_c (MPa)	Cohesion c (MPa)	Internal friction angle ϕ (°)
Mudstone	Site	1.8	2	0.35	7	600	25
	Mode	1.8	0.94	0.35	0.23	20	25
Sandstone	Site	2.5	8400	0.2	62	1	42
	Mode	2.5	280	0.2	1.2	0.1	42

486

487

Table. 4 Effect of water content on shear strength parameters

Water content (%)	Internal friction angle (°)	Change rate (%)	Cohesion (kPa)	Change rate (%)
-------------------	-----------------------------	-----------------	----------------	-----------------

6	18.61	\	54.8	\
9	21.7	-11.81	78.66	43.53
12	19.12	-22.32	55.62	1.5
15	19.02	-22.7	51.91	-5.27
18	17.68	-28.17	15.24	-72.2

488

489

Table. 5 Effect of immersion time on shear strength parameters.

Immersing time (h)	Internal friction angle (°)	Change rate (%)	Cohesion (kPa)	Change rate (%)
0h	22.24	\	50.91	\
1h	16.79	-40.53	15.22	-70.11
3h	16.71	-40.81	13.25	-73.98
6h	17.84	-36.84	9.69	-80.98
12h	17.69	-37.35	9.09	-82.15
24h	19.81	-29.84	10.83	-78.74
48h	18.26	-35.33	12.32	-75.81
96h	16.38	-41.98	10.28	-79.8

490

491

Table. 6 Parameter value for calculation

Conditions	Gravity	The inclination of sliding	Water gravity	Internal friction angle	Cohesion
	γ (kN/m ³)	surface θ (°)	γ_w (kN/m ³)	φ (°)	c (kPa)
Natural state	21	16	10	22.4	54.8
Only groundwater	21	16	10	16.4	10.3
Rainstorm	21	16	10	16.4	10.3

492

493

Table. 7 Calculating results of the factor of safety (F_s) with various depths of groundwater

Conditions	Natural state (no groundwater)	Only sliding surface in the saturated zone	Water depth to the sliding surface (m)						
			1	5	10	15	20	25	30
F_s	1.59	1.055	1.051	1.034	1.004	0.982	0.961	0.939	0.916

494

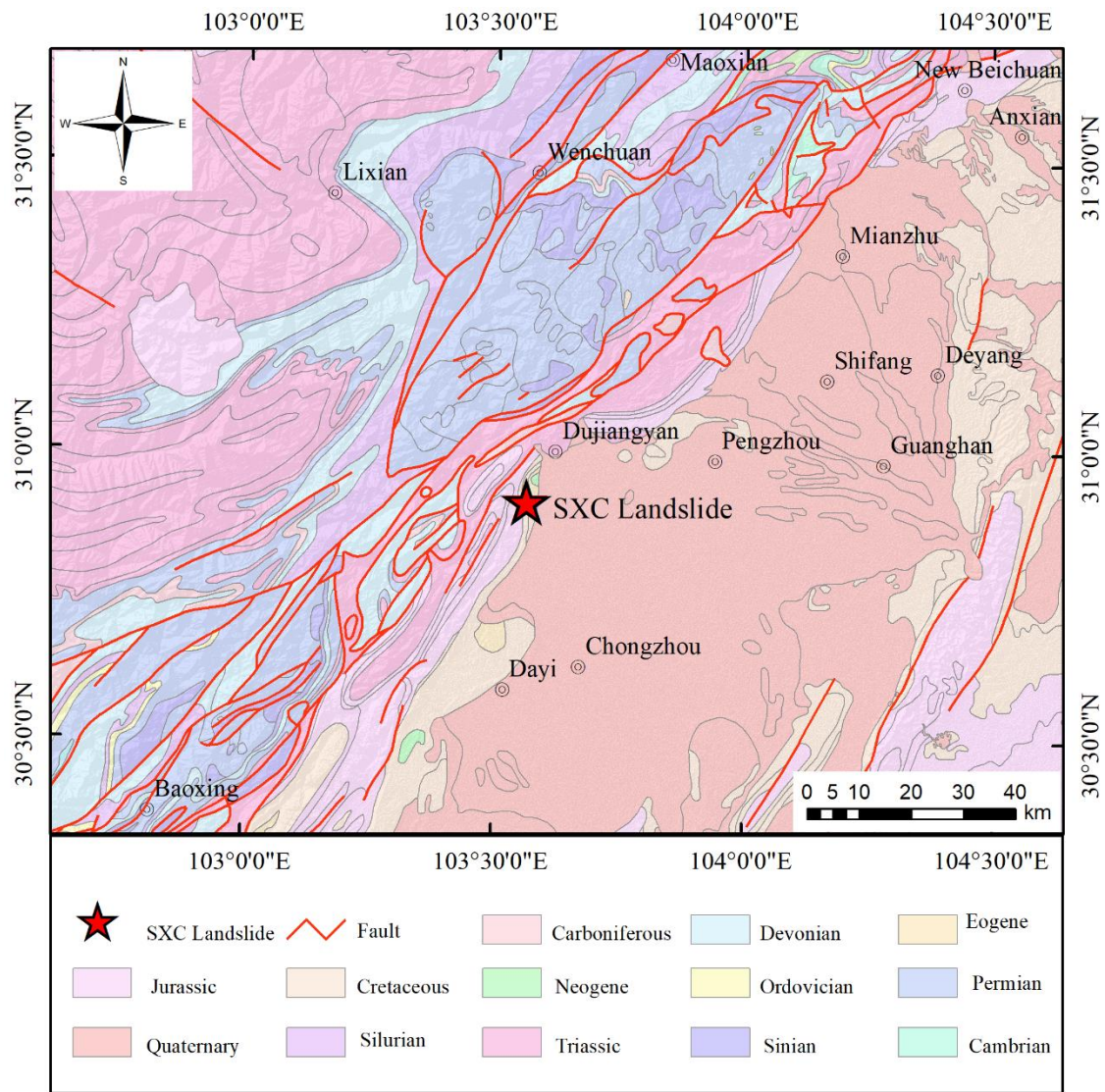


Fig. 1 Geologic setting of the study area

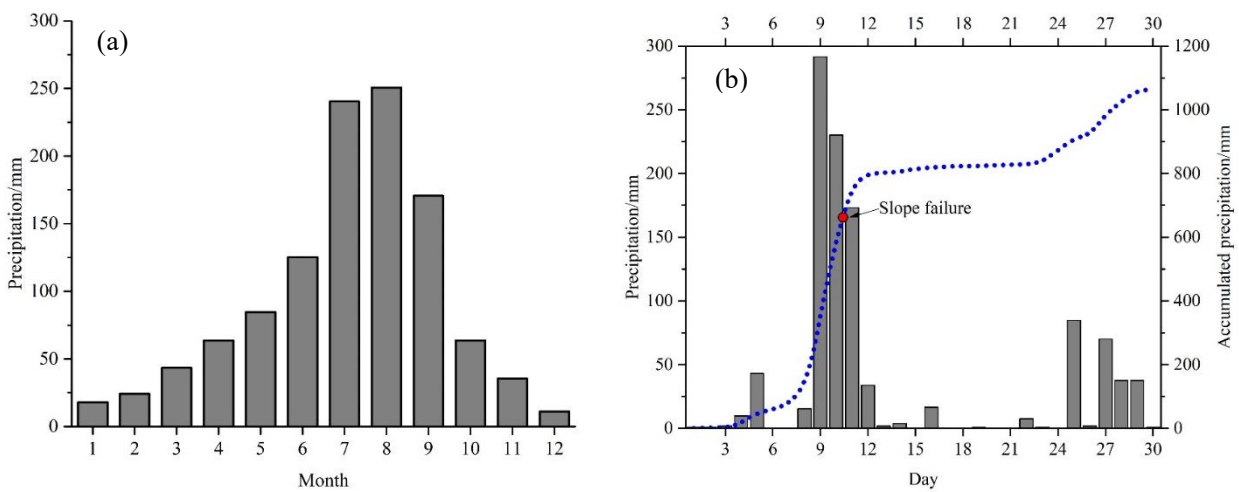


Fig. 2 Diagram of mean month precipitation at Dujiangyan from 1987 to 2012 (a) and precipitation and accumulated precipitation before and after the initiation of SXC landslide (b)

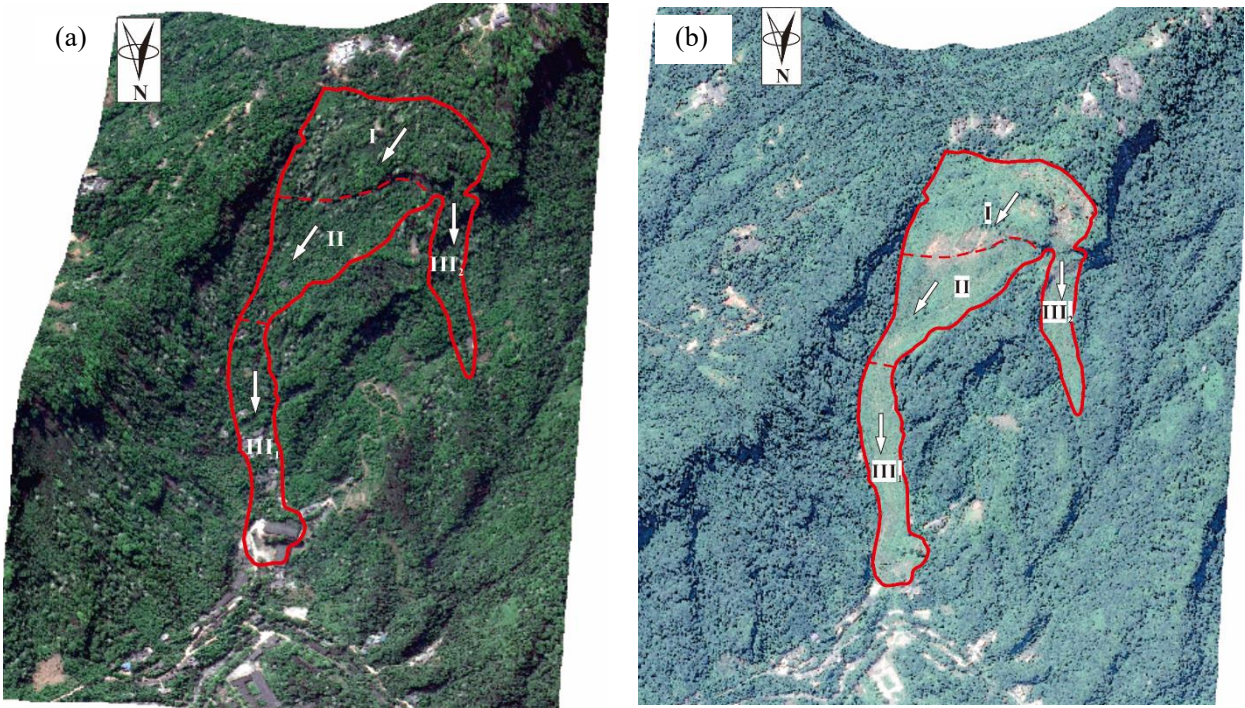
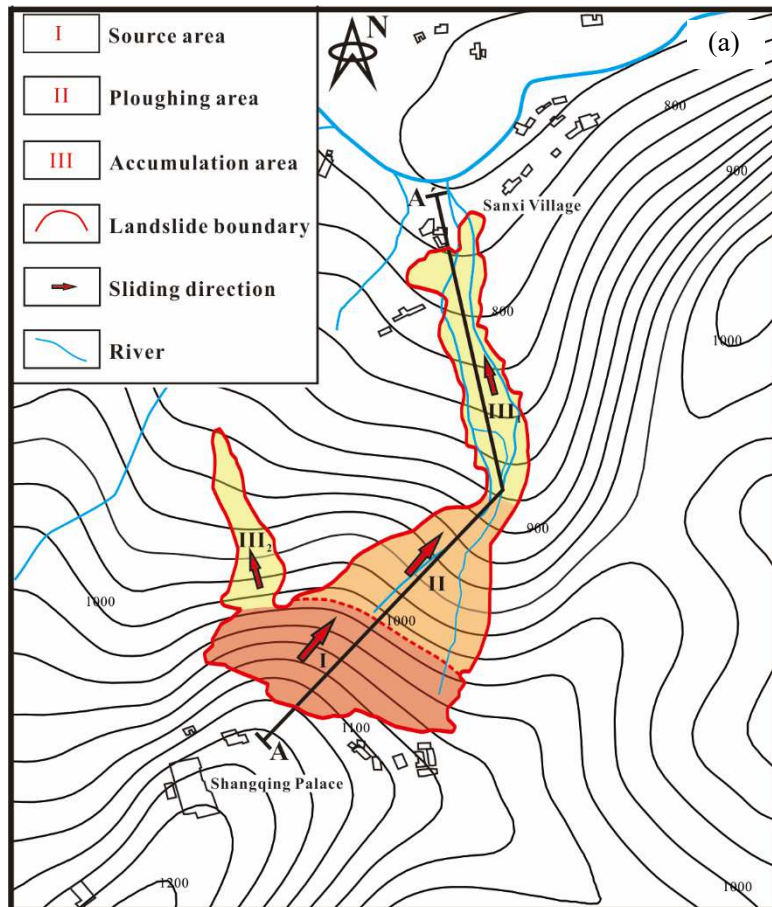


Fig. 3 Pre-sliding image on April 17th, 2013 (a) and post-sliding image on June 5th, 2016 (b)



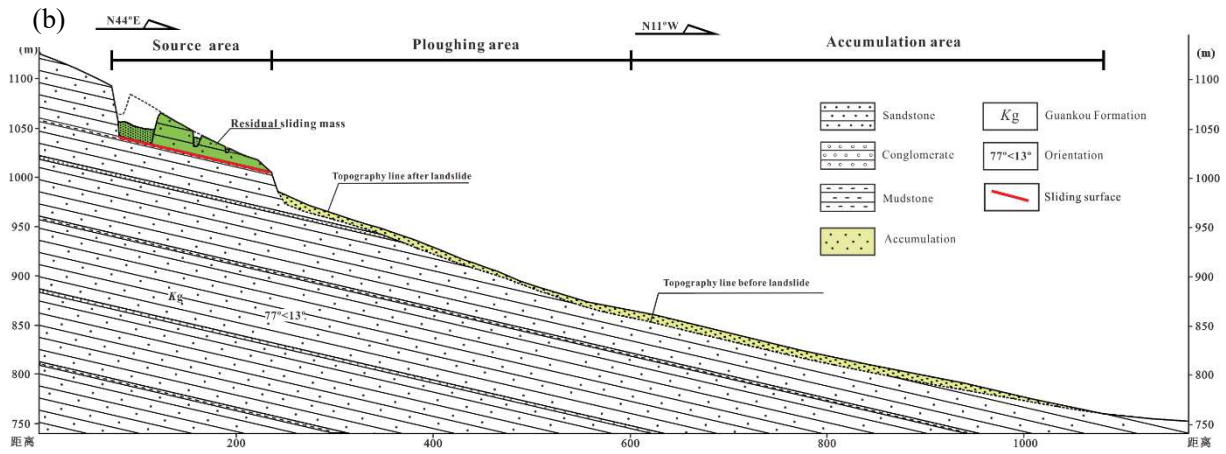
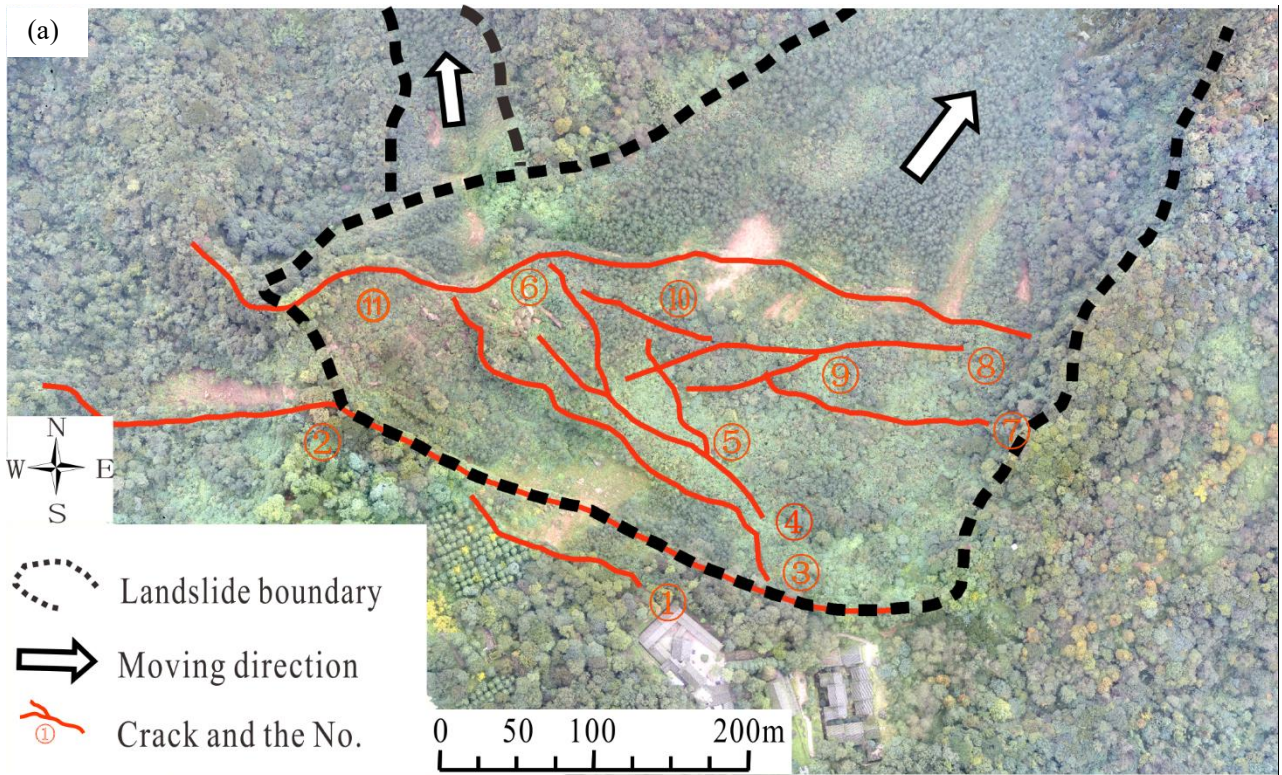


Fig. 4 SXC landslide map (a) and longitudinal profile of the landslide area (b)

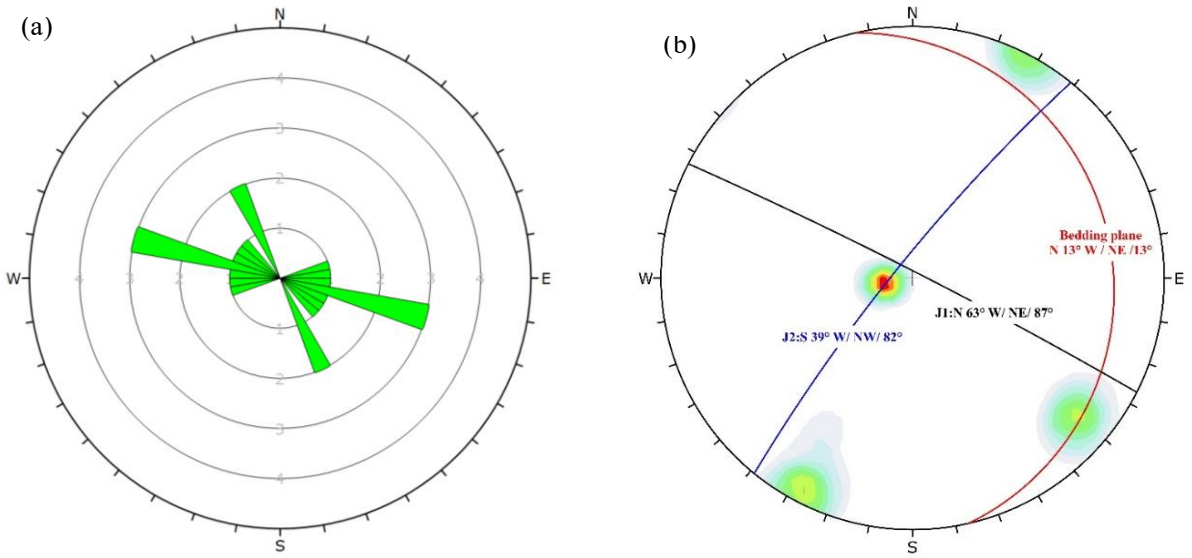
502

503



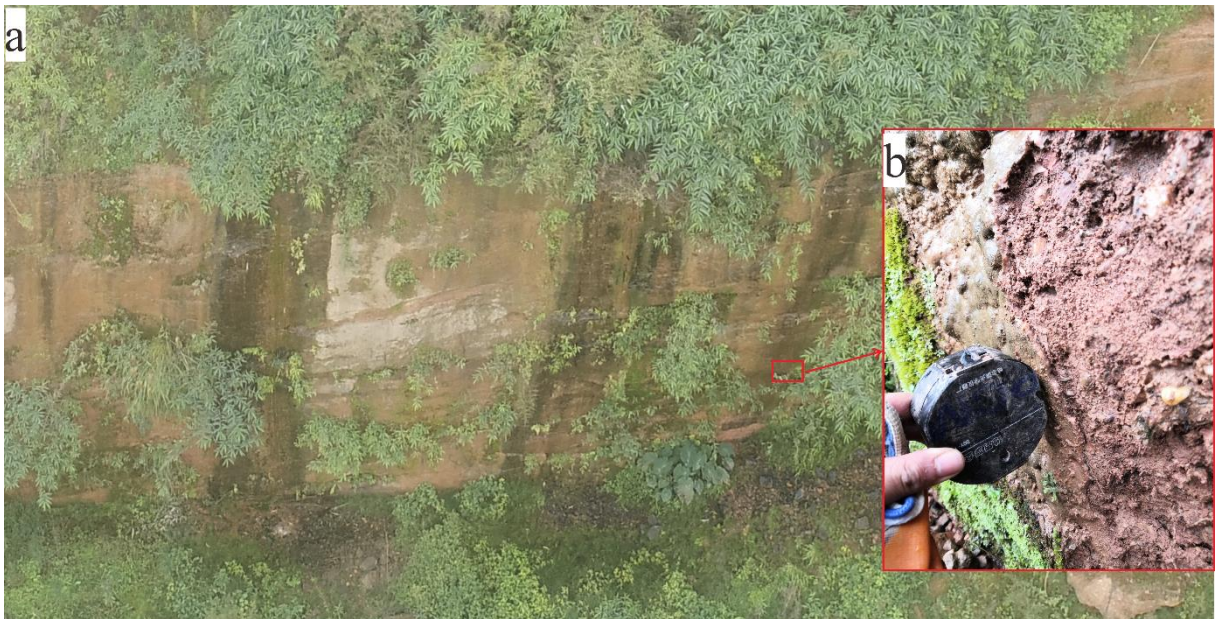
504
505
506

Fig. 5 The distribution of tension cracks in the source area (a), typical tension crack in the middle of residual sliding mass (b) and depression belt (c)



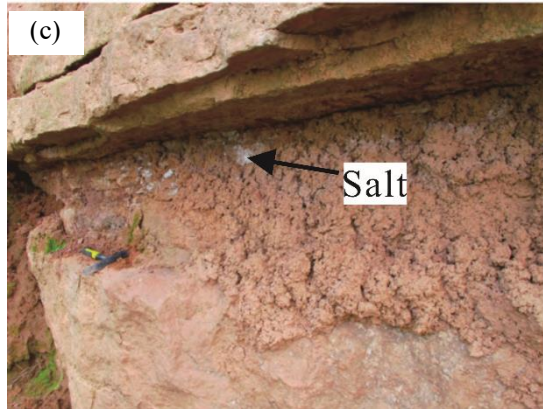
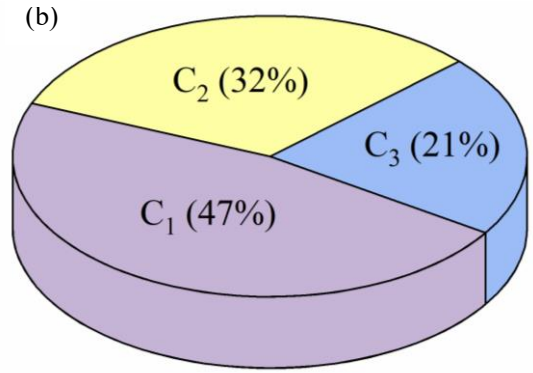
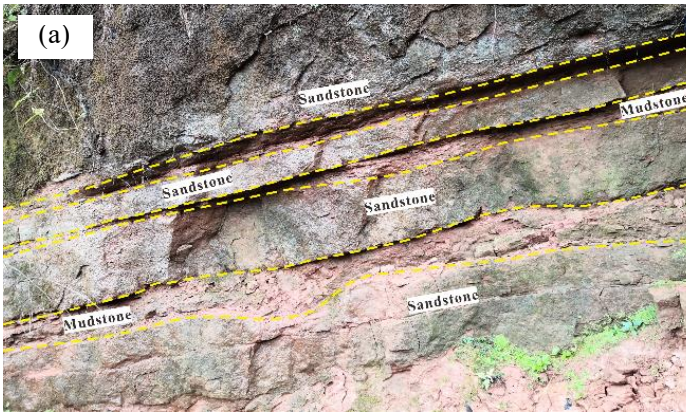
507
508

Fig. 6 Rose diagram of the tension crack strike (a) and stereographic projection of joints in the source area (b)

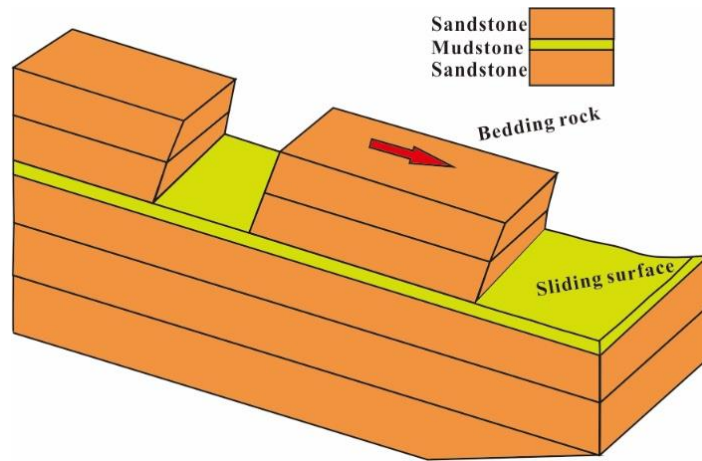


509
510
511

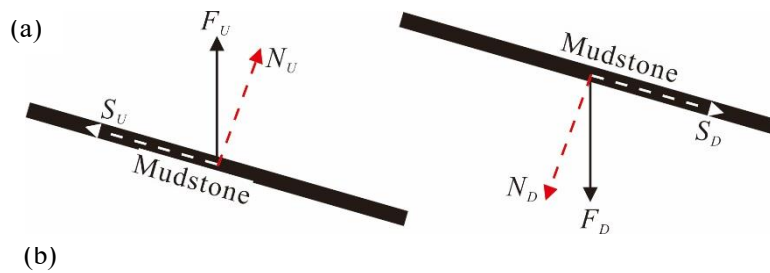
Fig. 7 Solution traces on the scarp surface (a) and a layer of calcareous film



512 Fig. 8 Strata characteristic in the source area (a), the statistical results of cracks in mudstone layer (b), C₁: gently inclined cracks, C₂:
 513 moderately -gently inclined cracks, C₃: steeply inclined cracks, and salt extracted from mudstone (c) (Du et al., 2016)
 514

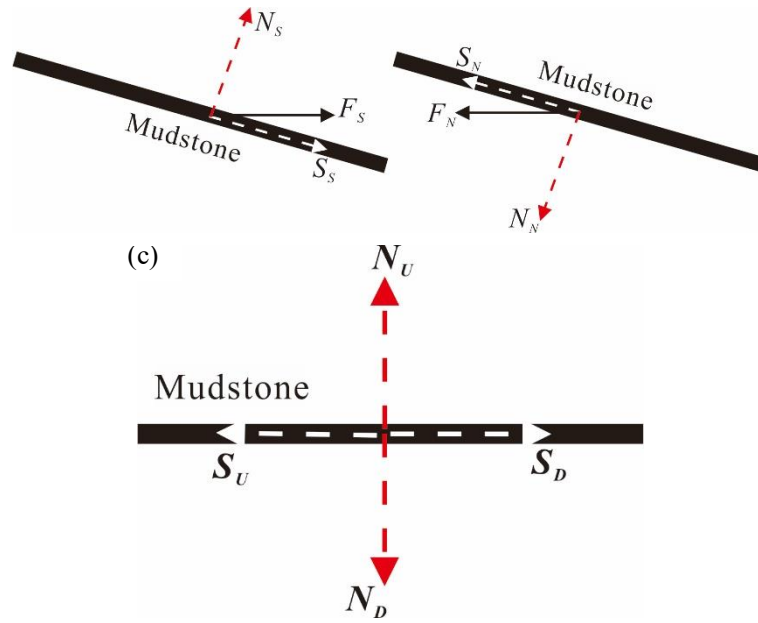


515
 516 Fig. 9 Diagram of strata, sliding surface, and slide block



518

519



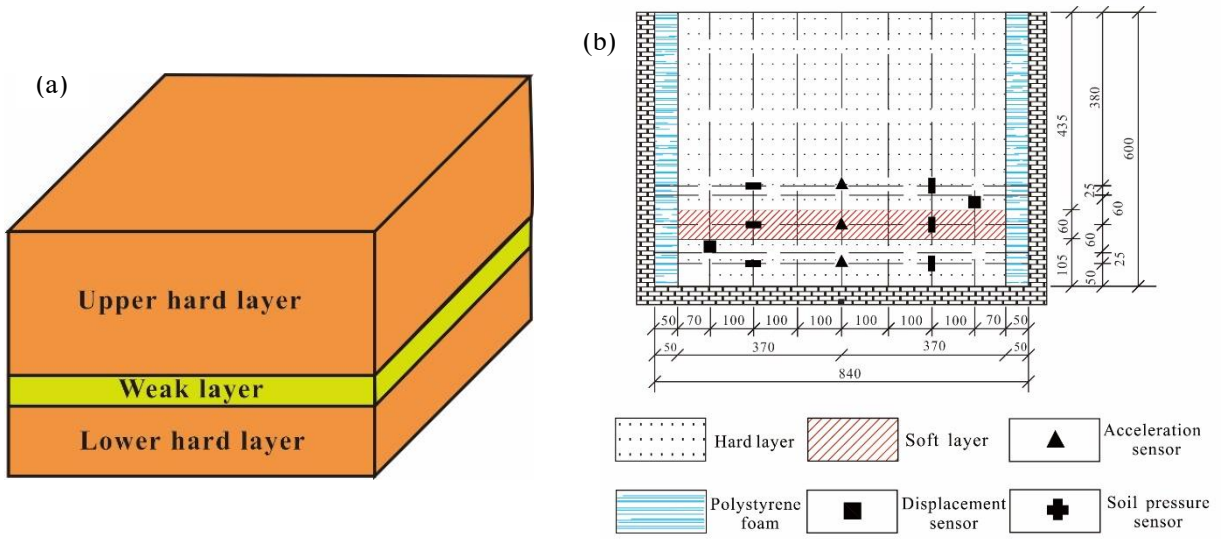
520

521

522

523

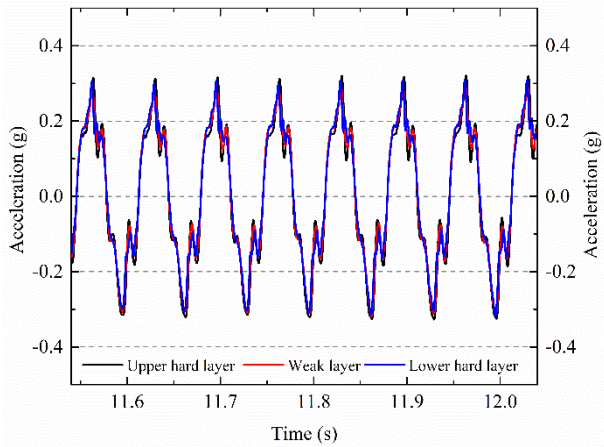
Fig. 10 Simplified mechanical mode: (a) decomposition of vertical seismic force, (b) decomposition of horizontal seismic force, and (c) seismic force composition



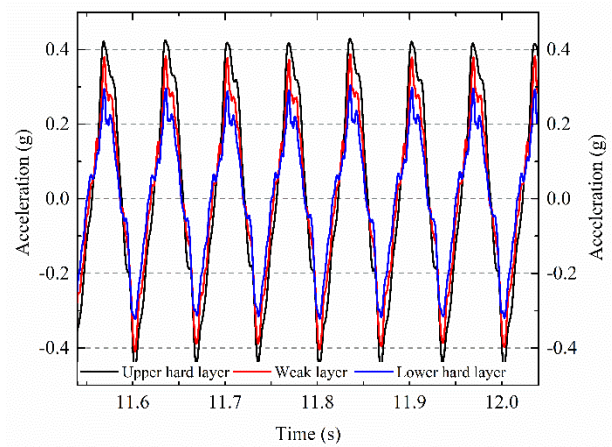
524

525

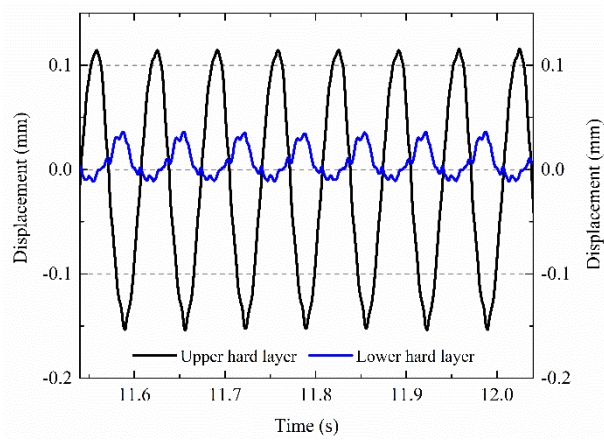
Fig. 11 A simplified model (a) and a shaking table test model and sensor placement scheme (b)



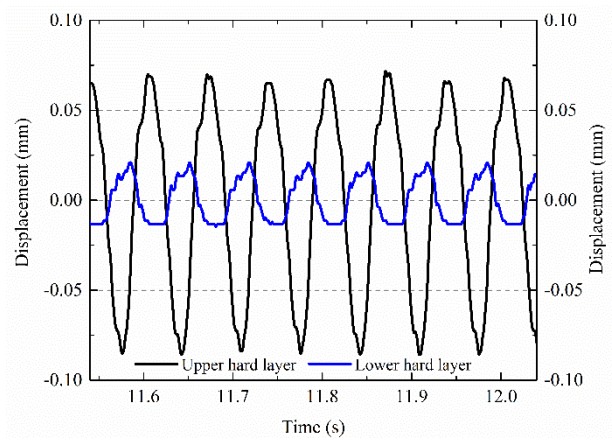
(a) Vertical vibration



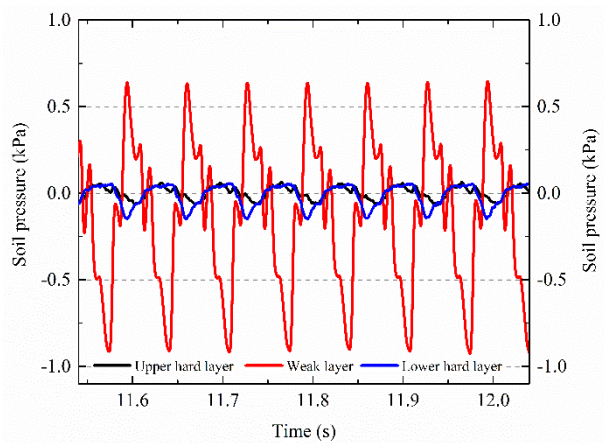
(b) Horizontal vibration



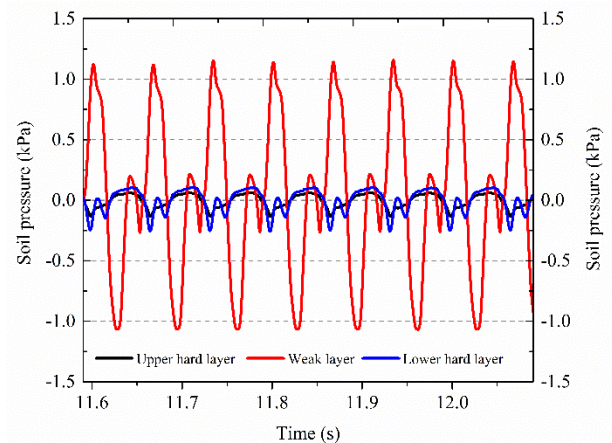
(c) Vertical vibration



(d) Horizontal vibration



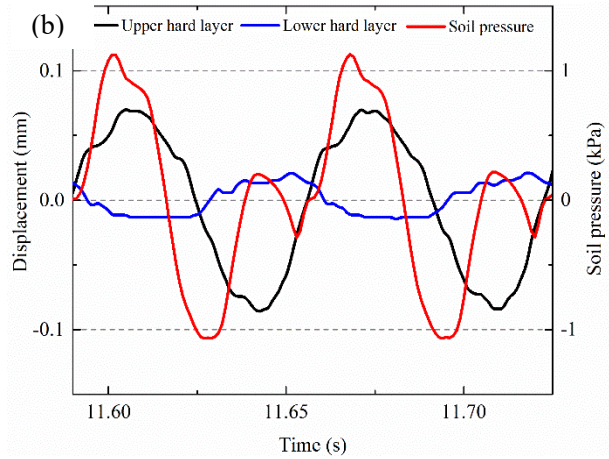
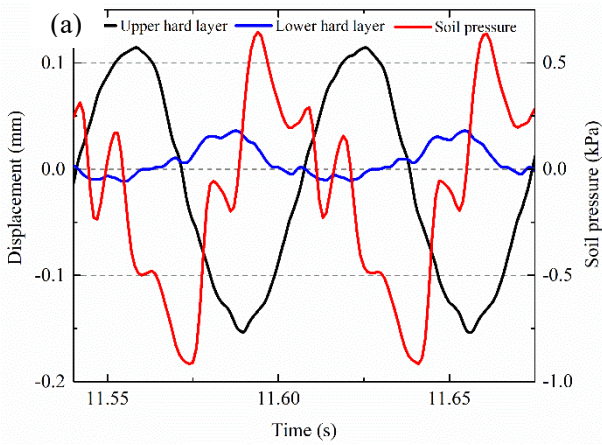
(e) Vertical vibration



(f) Horizontal vibration

Fig. 12 Shaking table test results

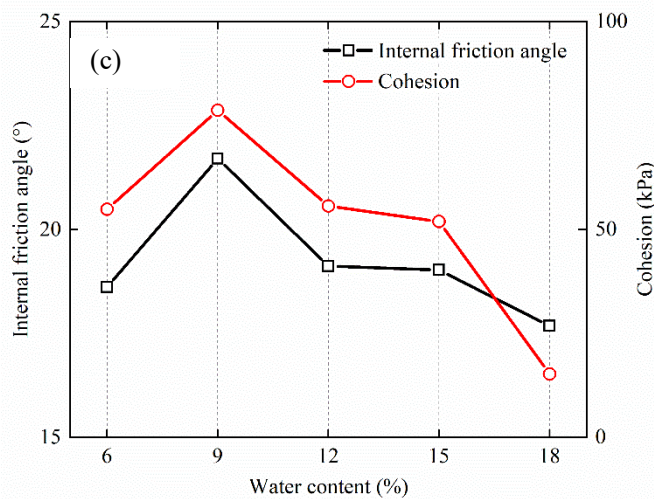
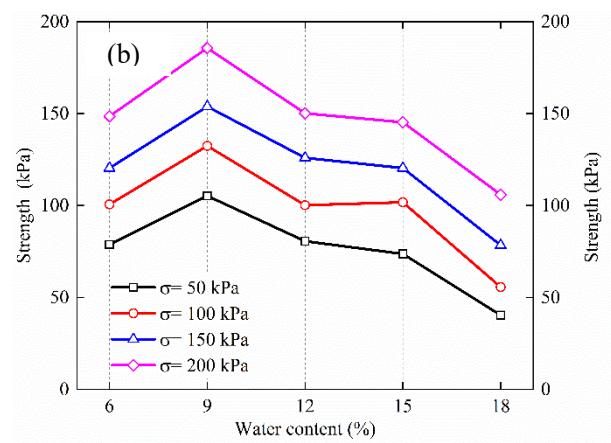
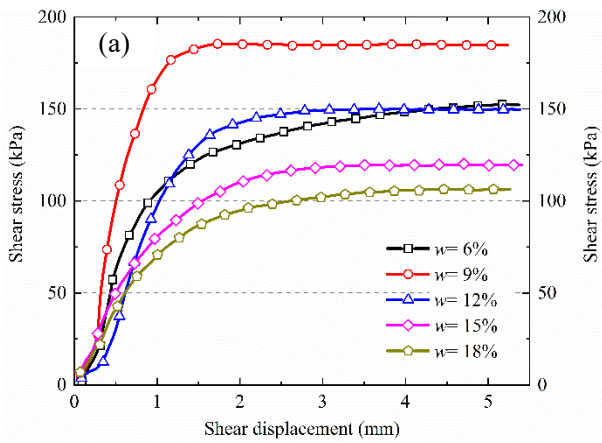
526
527



528

Fig. 13 Curves of displacement, soil pressure versus time: (a) vertical vibration, and (b) horizontal vibration

529

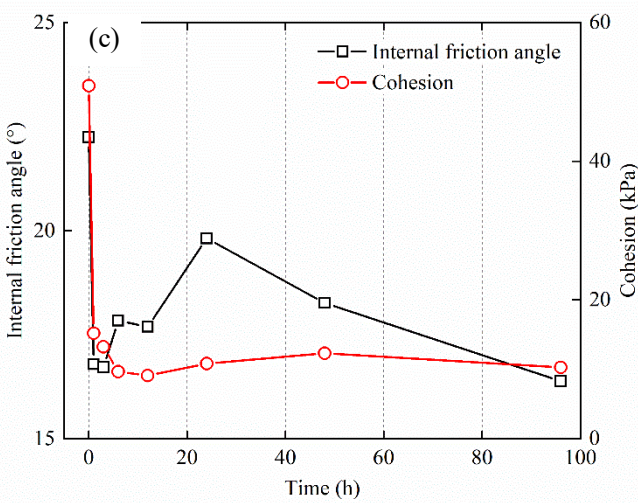
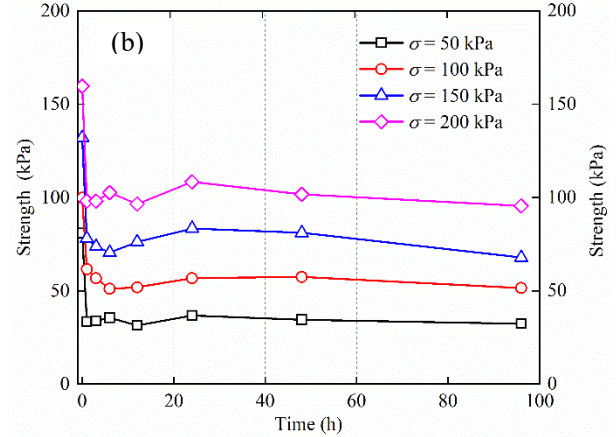
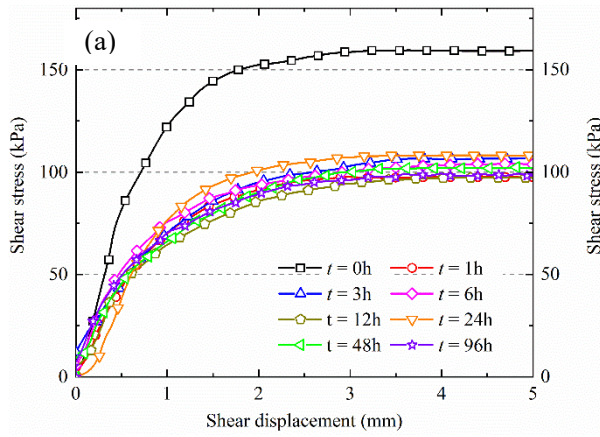


530

531

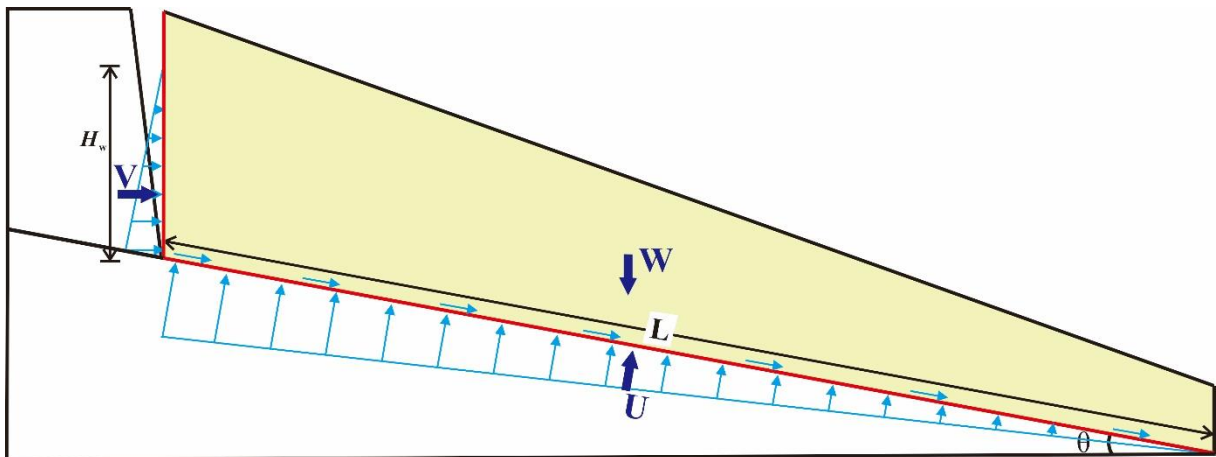
Fig. 14 Direct shear test results for samples with different water contents: (a) shear stress versus displacement curves, (b) shear strength versus water content curves, and (c) internal friction angle and cohesion versus water content curves

532



533 Fig. 15 Direct shear test results for samples with different immersion times: (a) shear stress versus displacement curves for $\sigma = 200 \text{ kPa}$,
 534 (b) shear strength versus water immersion time curves, (c) internal friction angle and cohesion versus immersion time curves

535



536

537

538

Fig. 16 Stability calculation of profile B-B'

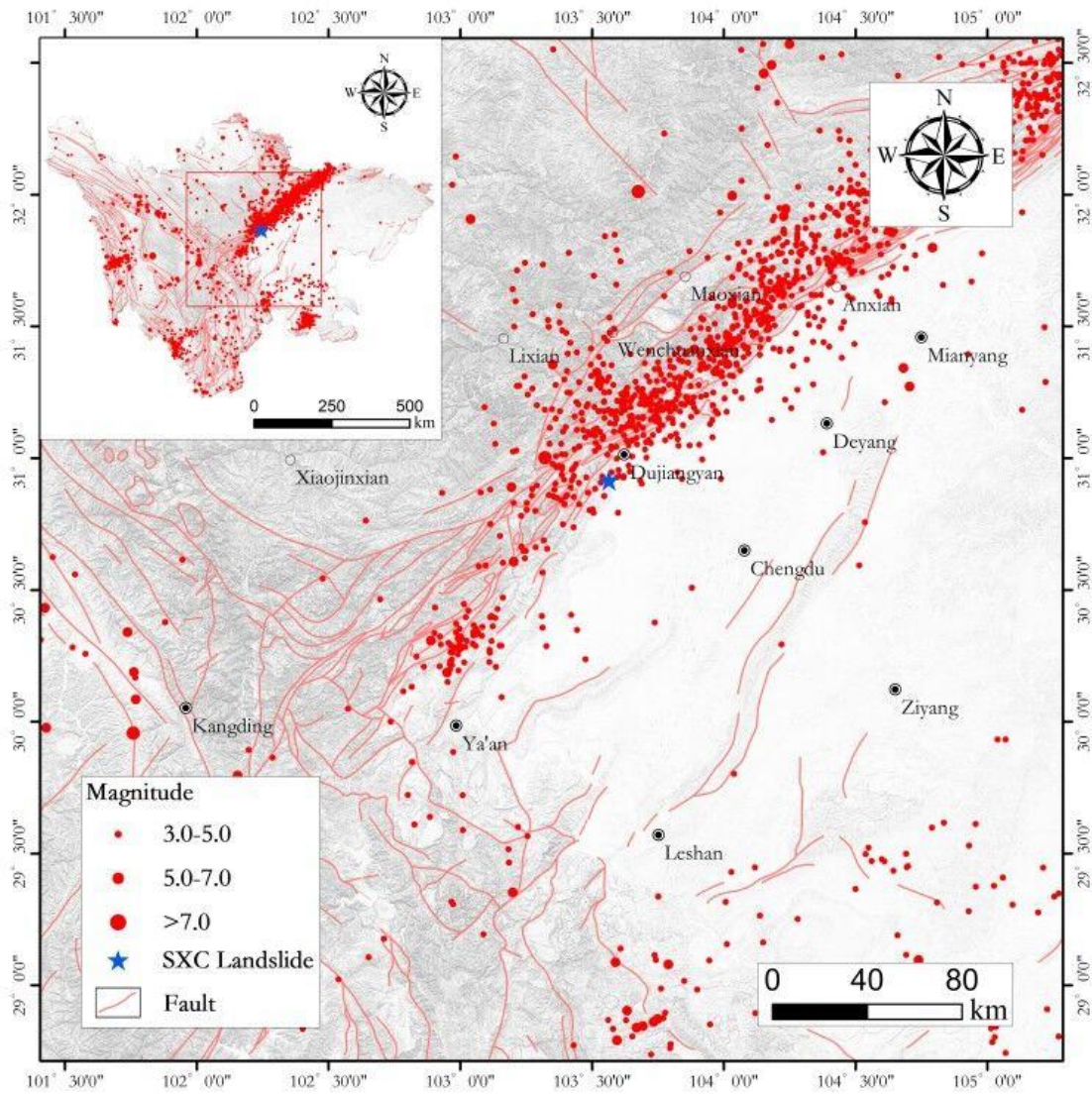


Fig. 17 Earthquake events occurring in the adjacent area since 1900

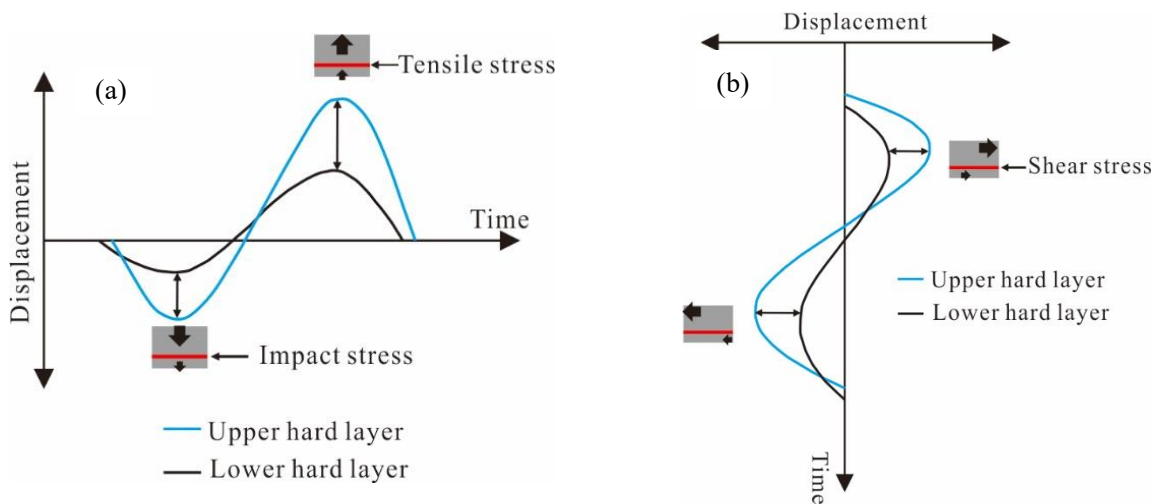
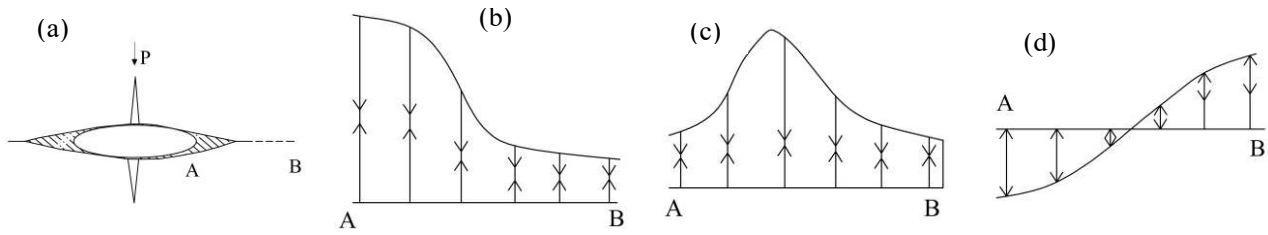
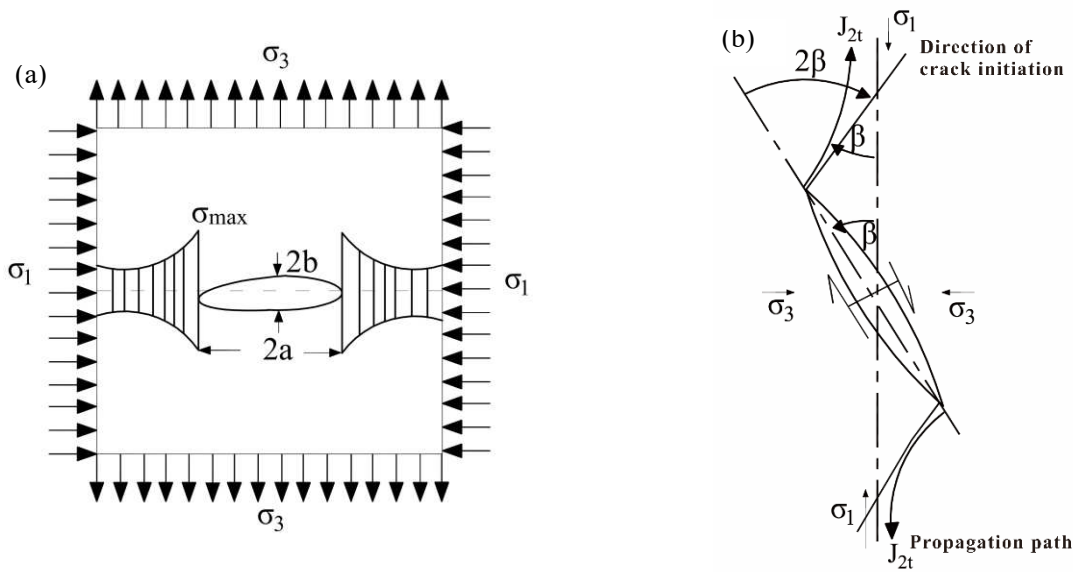


Fig. 18 Diagram of incompatible deformation in the model: (a) impact and tension stresses, (b) shear stress



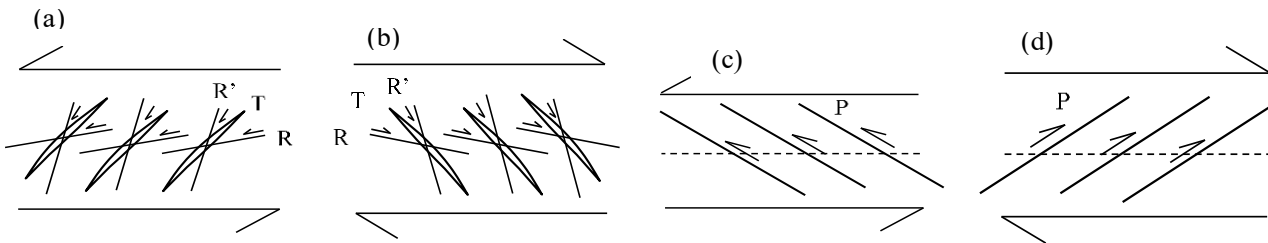
544 Fig. 19 Mechanisms of crack propagation under compression stress (modified by Lajtai 1977): (a) the tension fracture pattern of the
 545 original crack, (b) the stress concentration position at the crack tip, (c) transfer of stress concentration position, and (d) residual tension
 546 stress

547



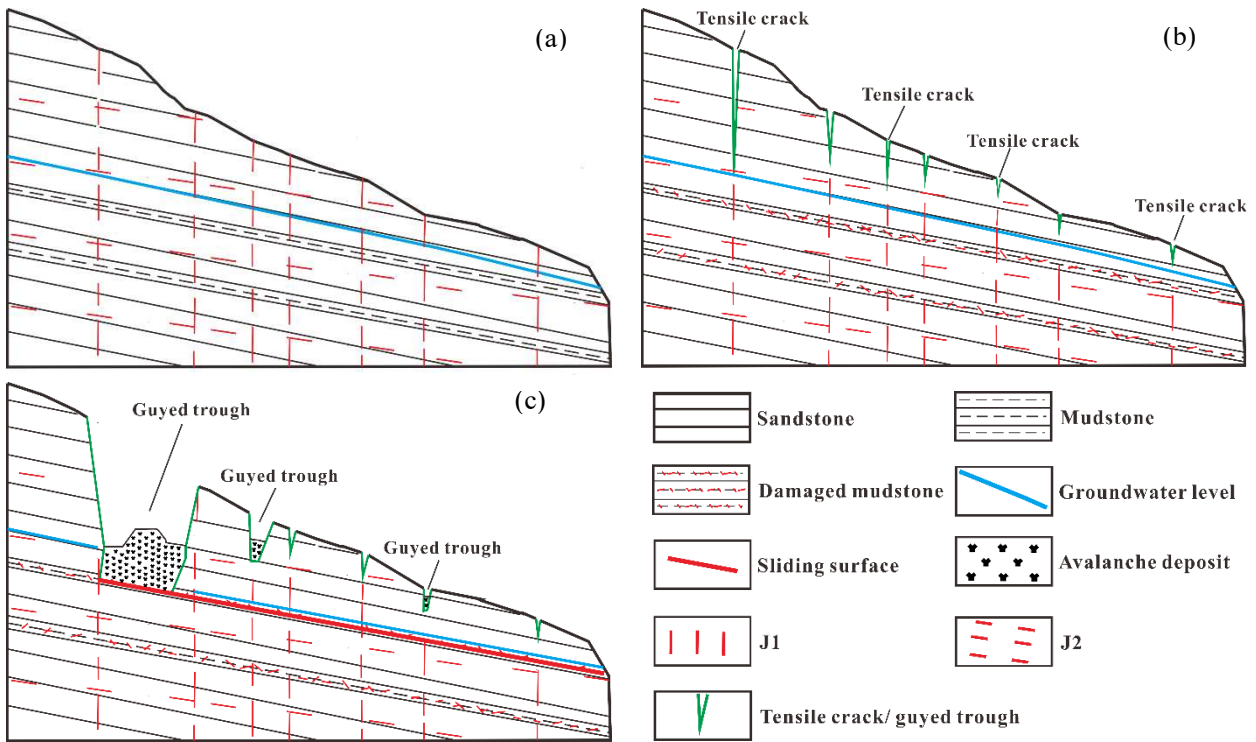
548 Fig. 20 Mechanisms of crack propagation under tension stress (a) and mechanisms of tension failure under compression stress (b)

549



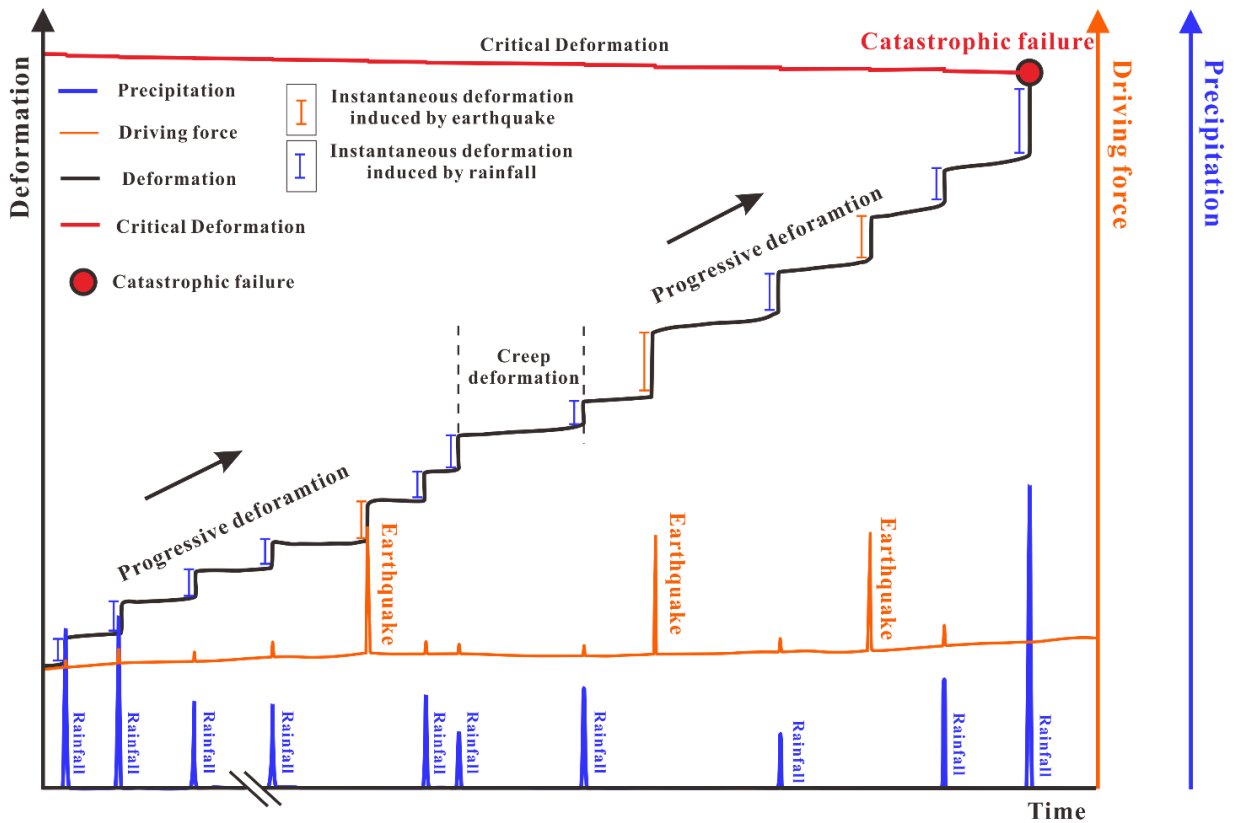
550 Fig. 21 Mechanisms of crack propagation under cyclic shear stress, a. sinistral tension cracks, b. dextral tension cracks, c sinistral
 551 compressive- torsion cracks, d dextral compressive- torsion cracks

552



553 Fig. 22 Formation and evolution process of the cracked slope, (a) original slope with joints (b) seismic cracks formed by historical
 554 earthquakes, (c) progressive deformation of slope and the formation of tension cracks under the combined influence of earthquake,
 555 rainfall and gravity

556



557 Fig. 23 Progressive deformation process of SXC slope under the influence of historical earthquakes, gravity and rainfall
 558

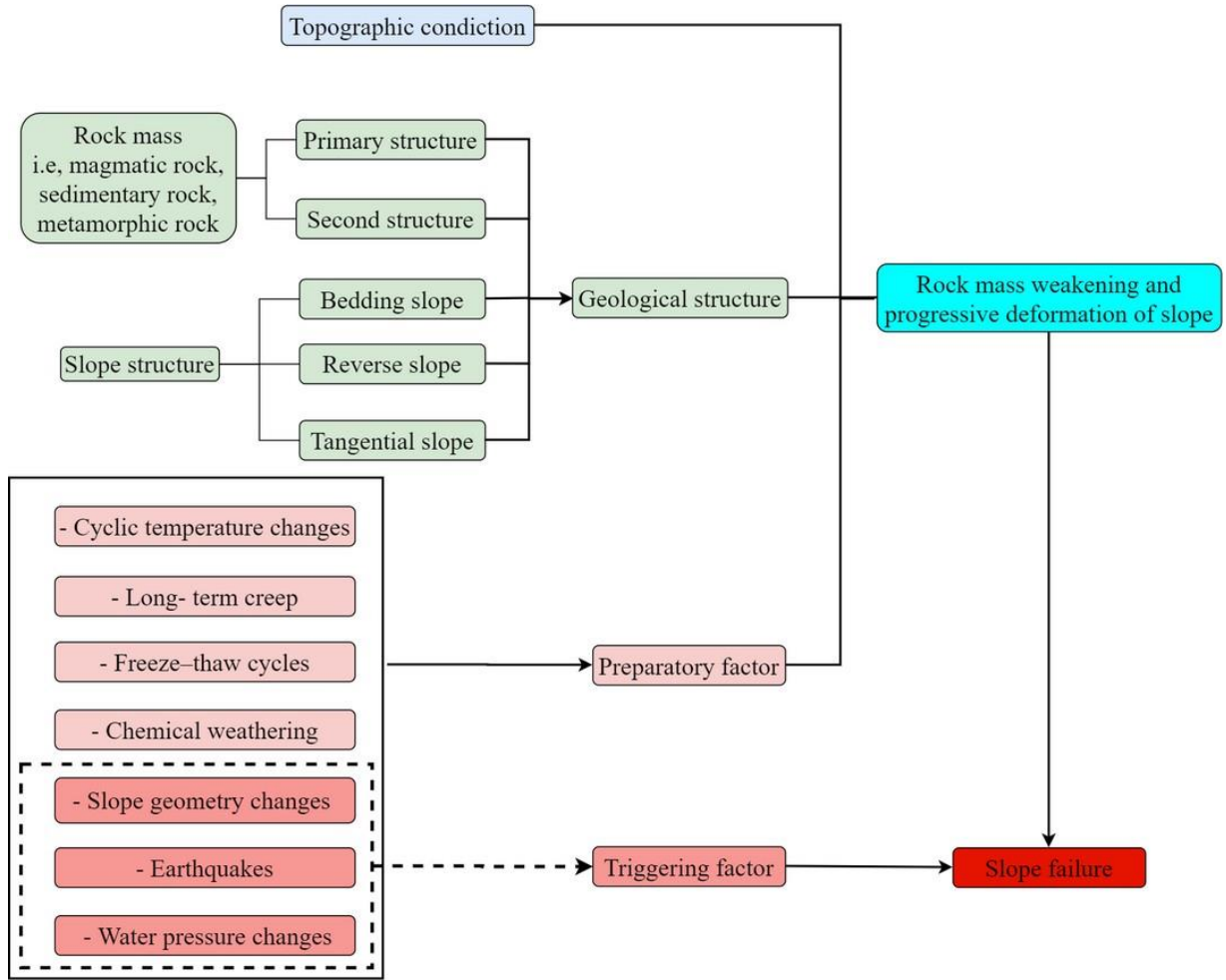


Fig. 24 Flowchart illustrating the rock mass weakening and progressive failure of slope

Figures

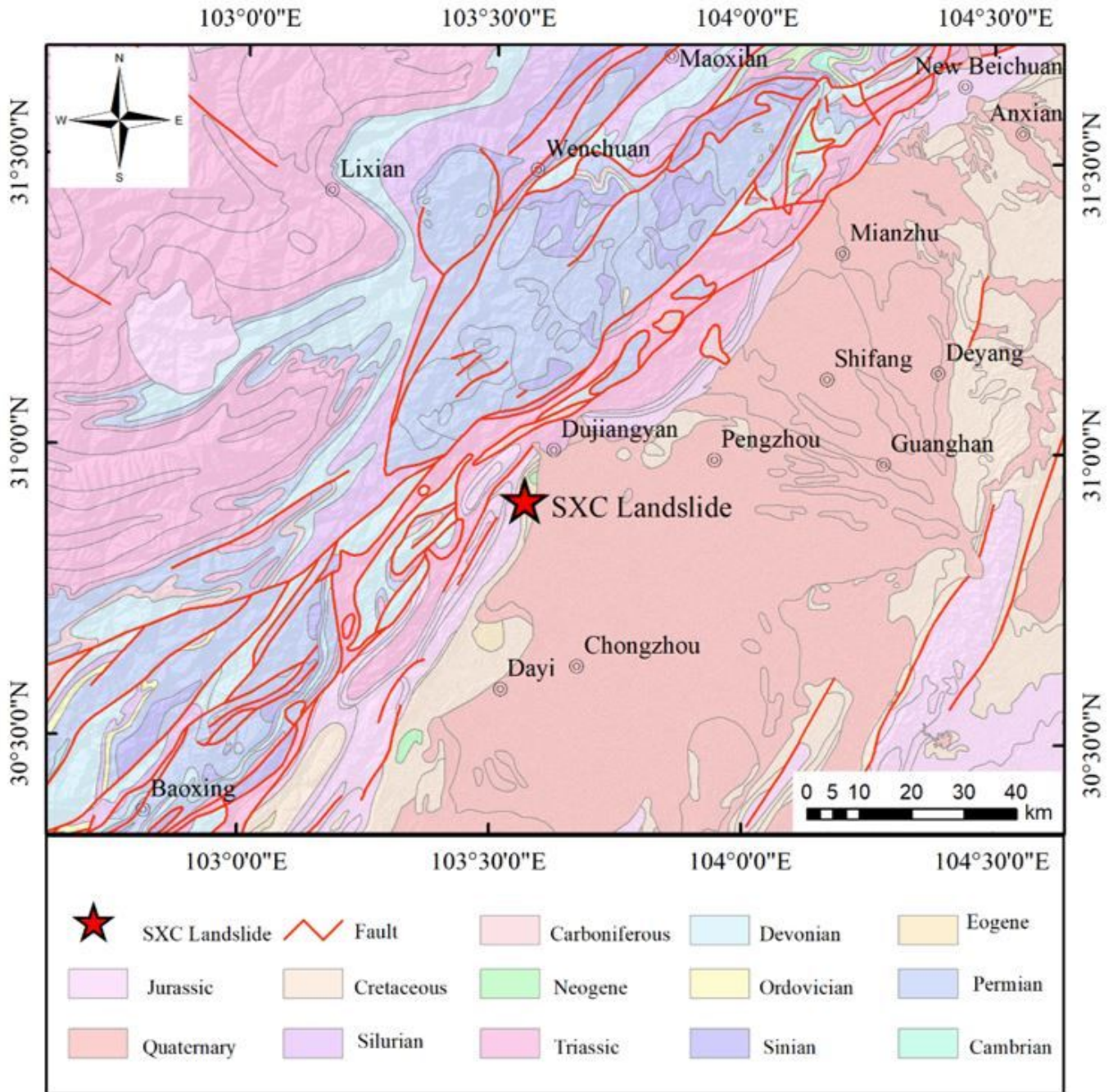


Figure 1

Geologic setting of the study area Note: The designations employed and the presentation of the material on this map do not imply the expression of any opinion whatsoever on the part of Research Square concerning the legal status of any country, territory, city or area or of its authorities, or concerning the delimitation of its frontiers or boundaries. This map has been provided by the authors.

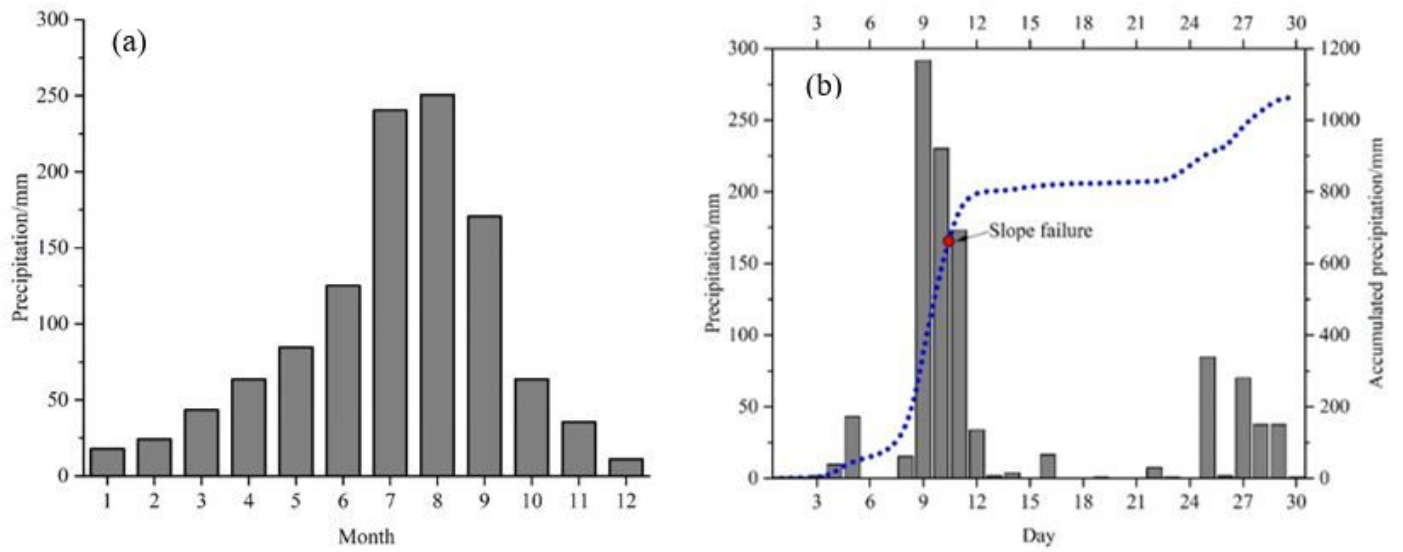


Figure 2

Diagram of mean month precipitation at Dujiangyan from 1987 to 2012 (a) and precipitation and accumulated precipitation before and after the initiation of SXC landslide (b)

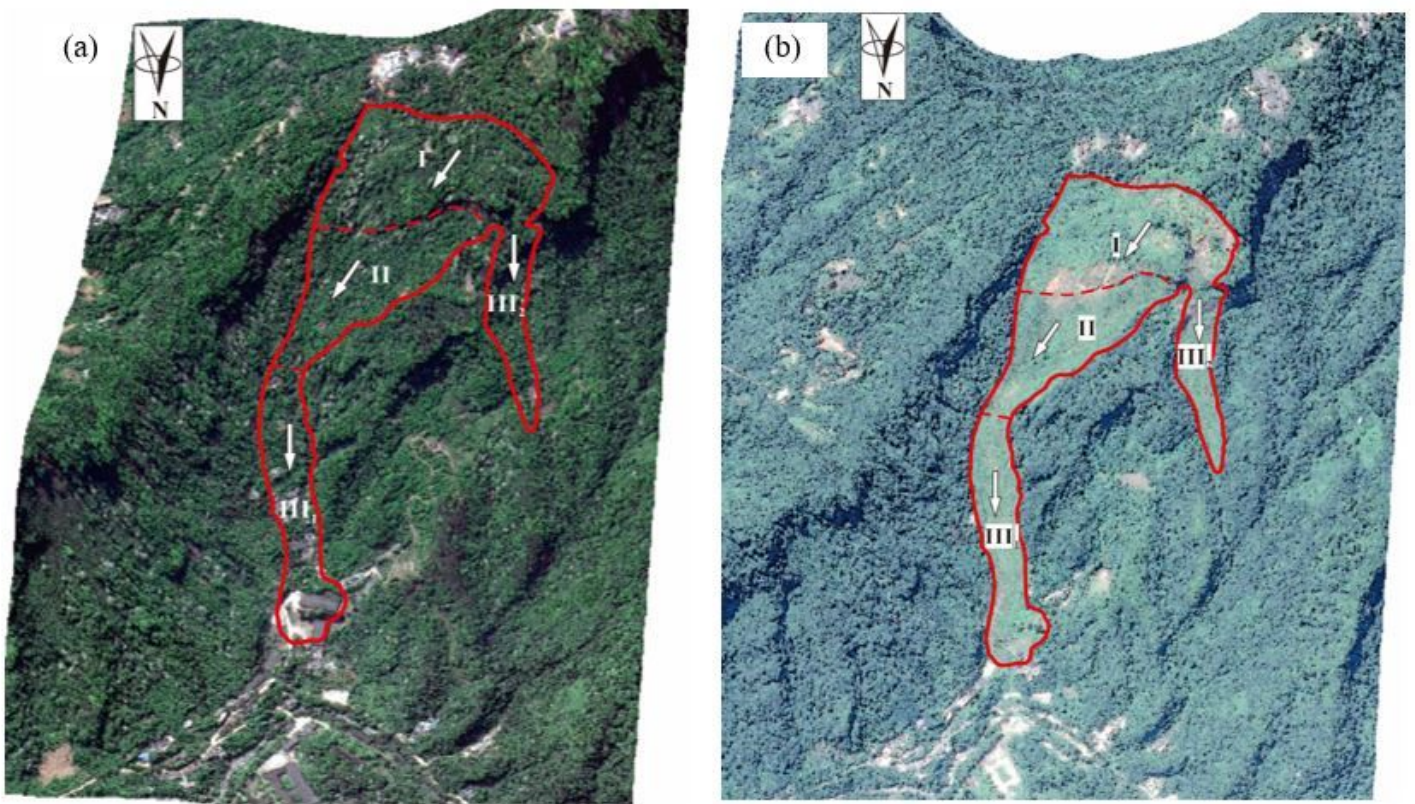


Figure 3

Pre-sliding image on April 17th, 2013 (a) and post-sliding image on June 5th, 2016 (b) Note: The designations employed and the presentation of the material on this map do not imply the expression of any opinion whatsoever on the part of Research Square concerning the legal status of any country, territory, city or area or of its authorities, or concerning the delimitation of its frontiers or boundaries. This map has been provided by the authors.

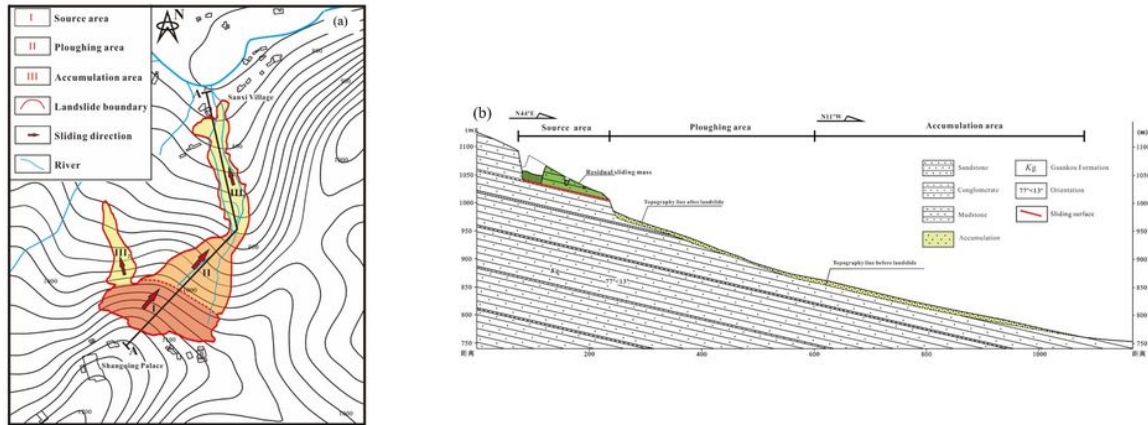


Figure 4

SXC landslide map (a) and longitudinal profile of the landslide area (b) Note: The designations employed and the presentation of the material on this map do not imply the expression of any opinion whatsoever on the part of Research Square concerning the legal status of any country, territory, city or area or of its authorities, or concerning the delimitation of its frontiers or boundaries. This map has been provided by the authors.

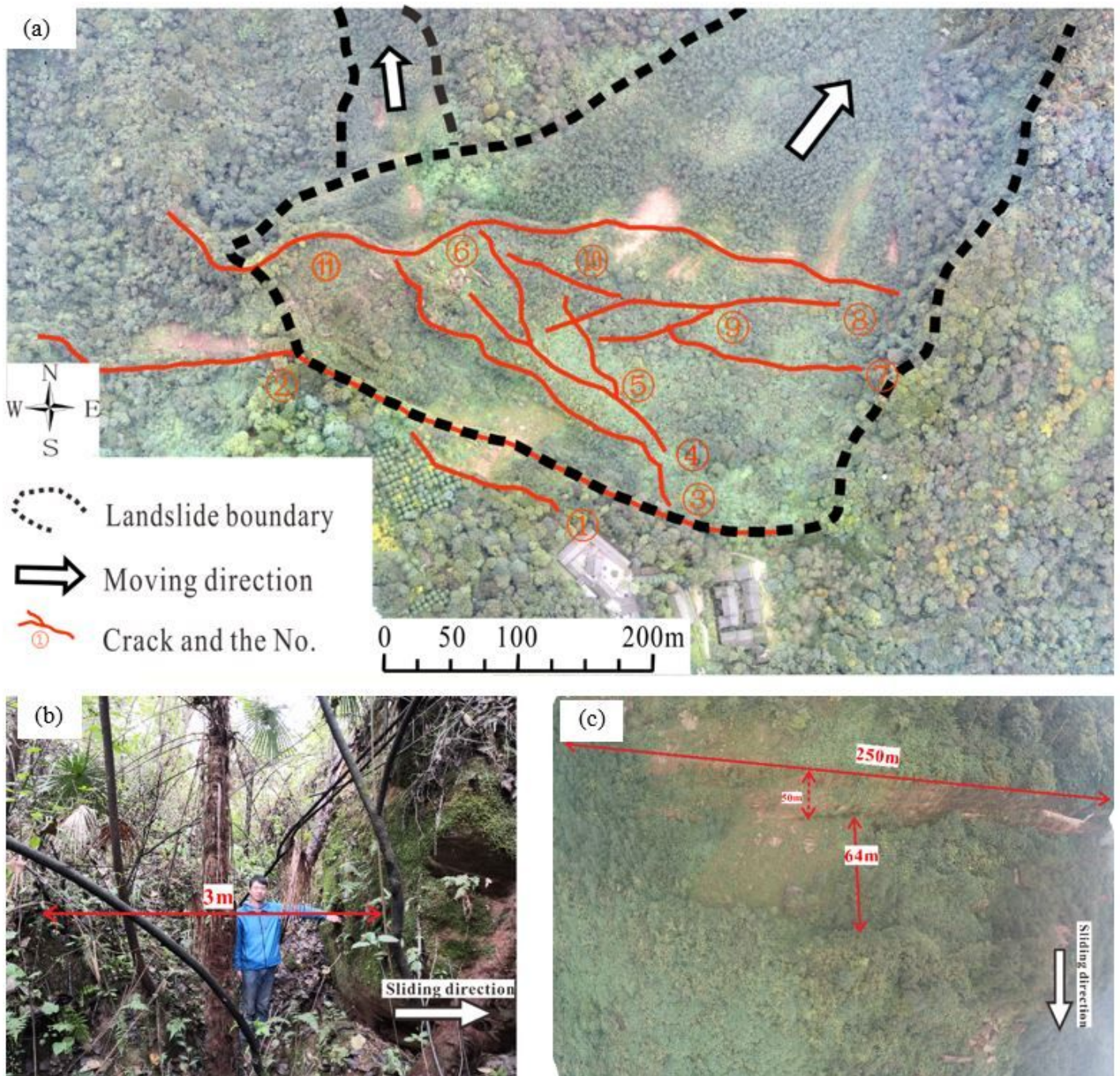


Figure 5

The distribution of tension cracks in the source area (a), typical tension crack in the middle of residual sliding mass (b) and depression belt (c) Note: The designations employed and the presentation of the material on this map do not imply the expression of any opinion whatsoever on the part of Research Square concerning the legal status of any country, territory, city or area or of its authorities, or concerning the delimitation of its frontiers or boundaries. This map has been provided by the authors.

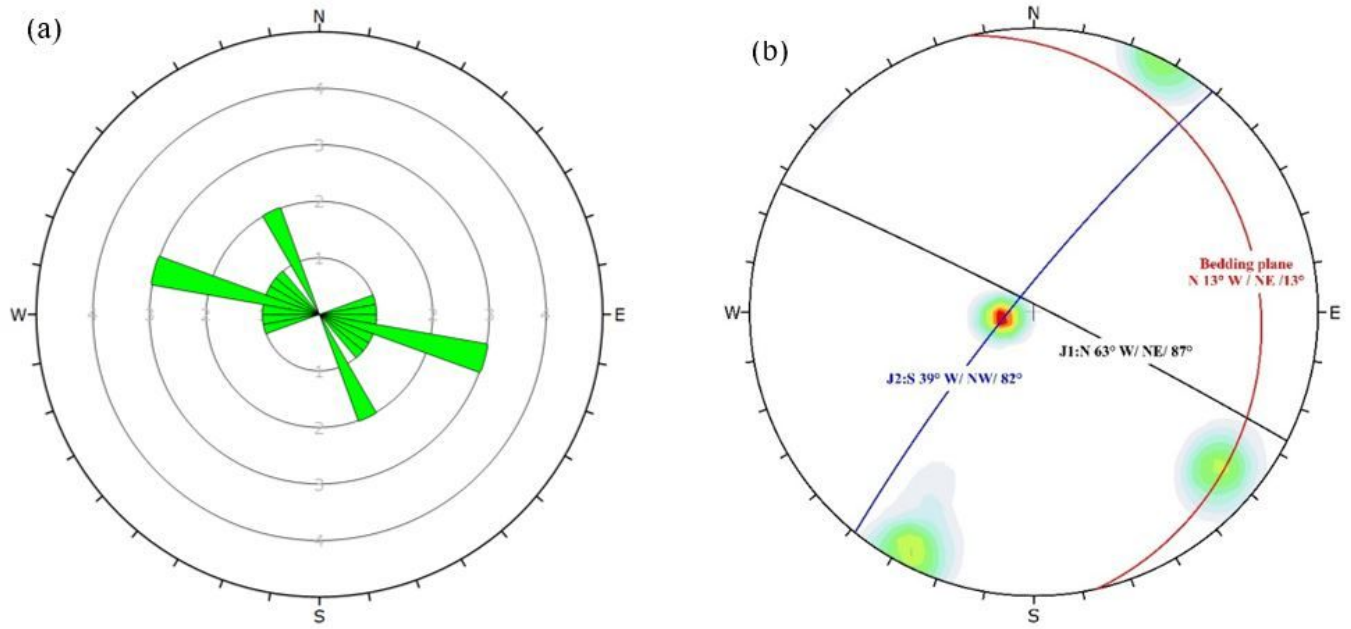


Figure 6

Rose diagram of the tension crack strike (a) and stereographic projection of joints in the source area (b)

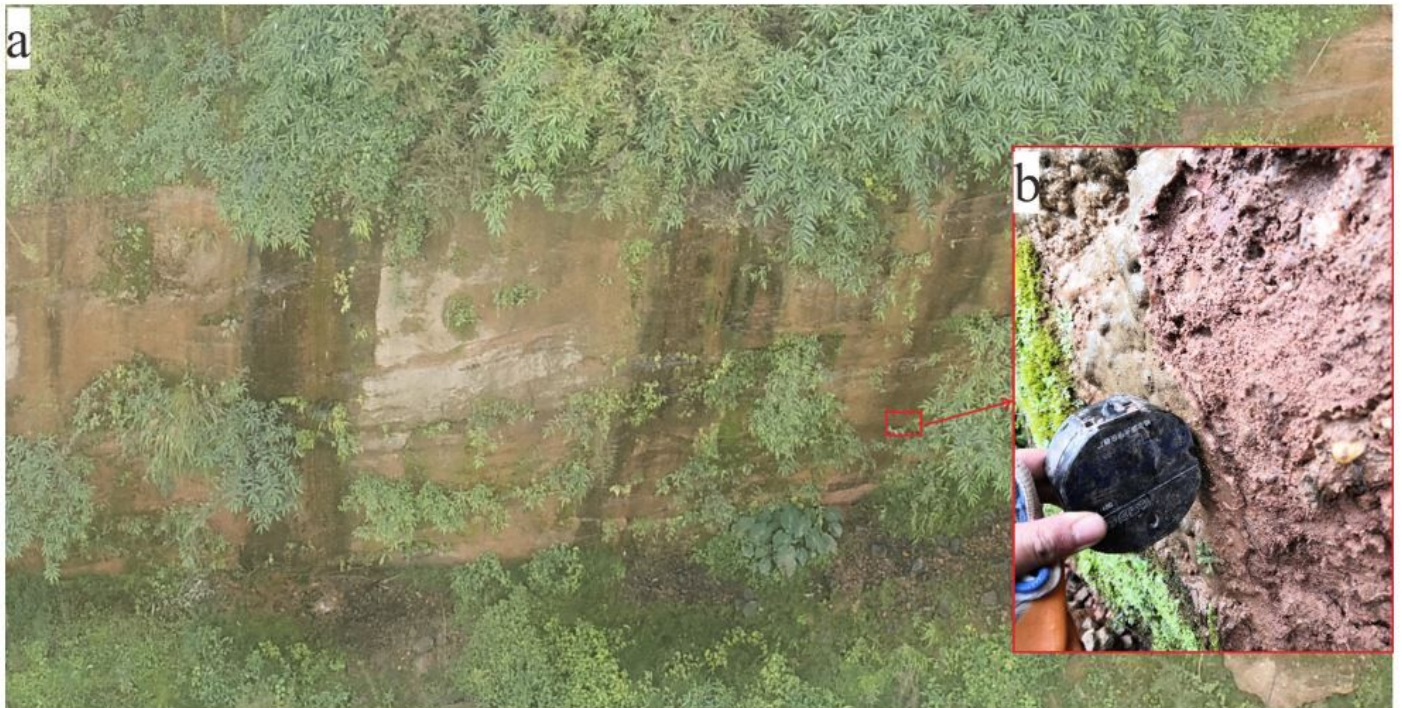


Figure 7

Solution traces on the scarp surface (a) and a layer of calcareous film

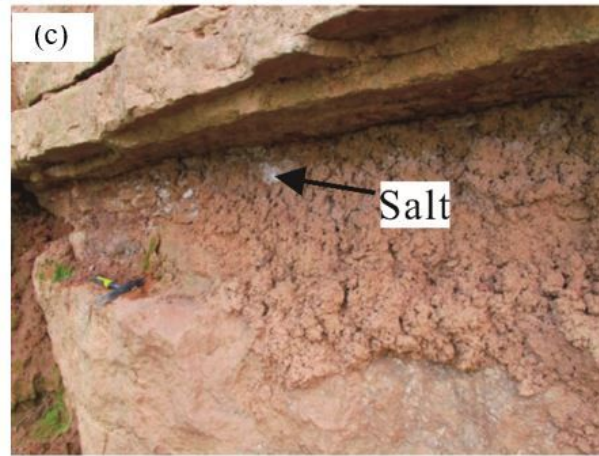
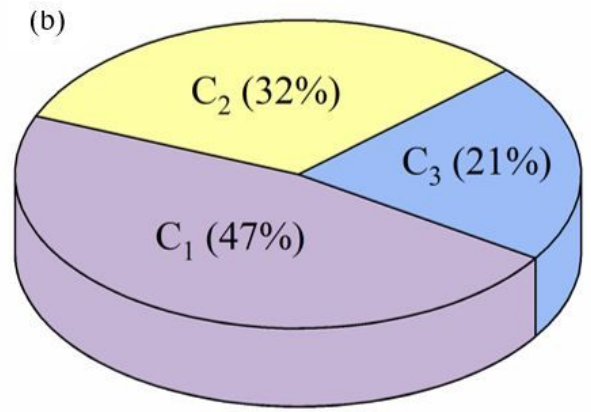
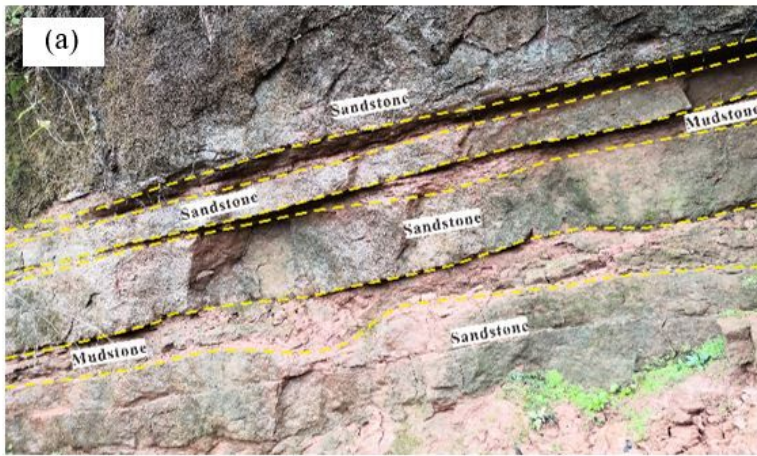


Figure 8

Strata characteristic in the source area (a), the statistical results of cracks in mudstone layer (b), C1: gently inclined cracks, C2: moderately-gently inclined cracks, C3: steeply inclined cracks, and salt extracted from mudstone (c) (Du et al., 2016)

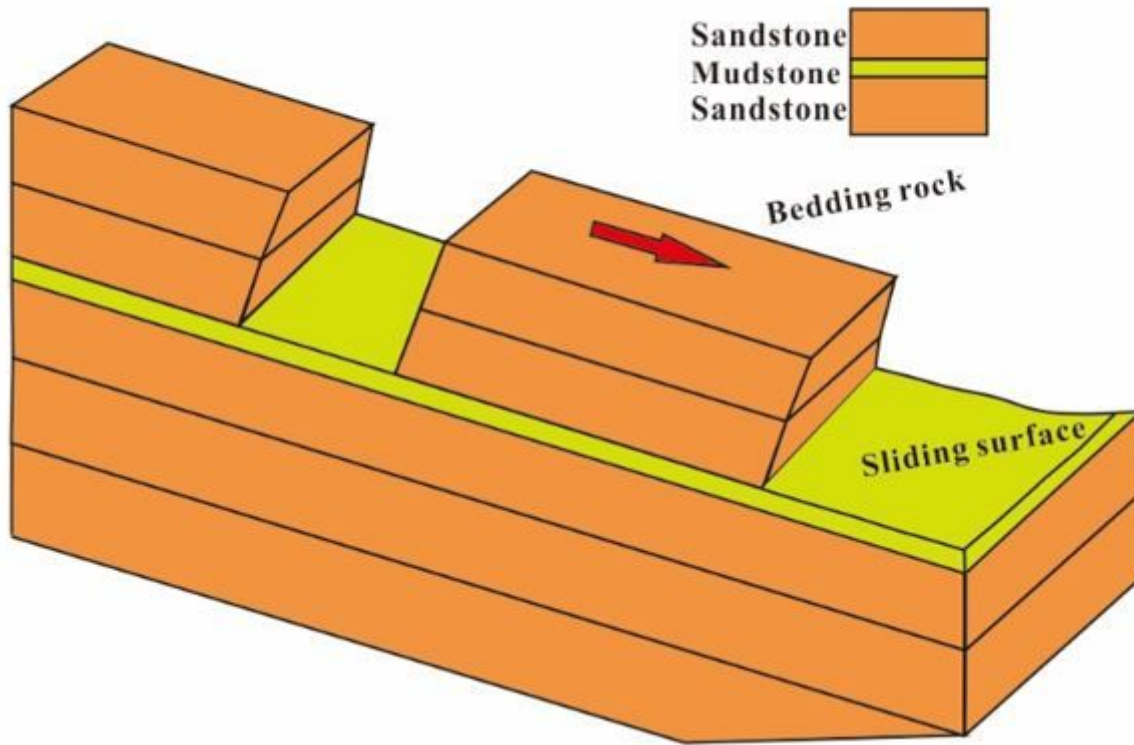


Figure 9

Diagram of strata, sliding surface, and slide block

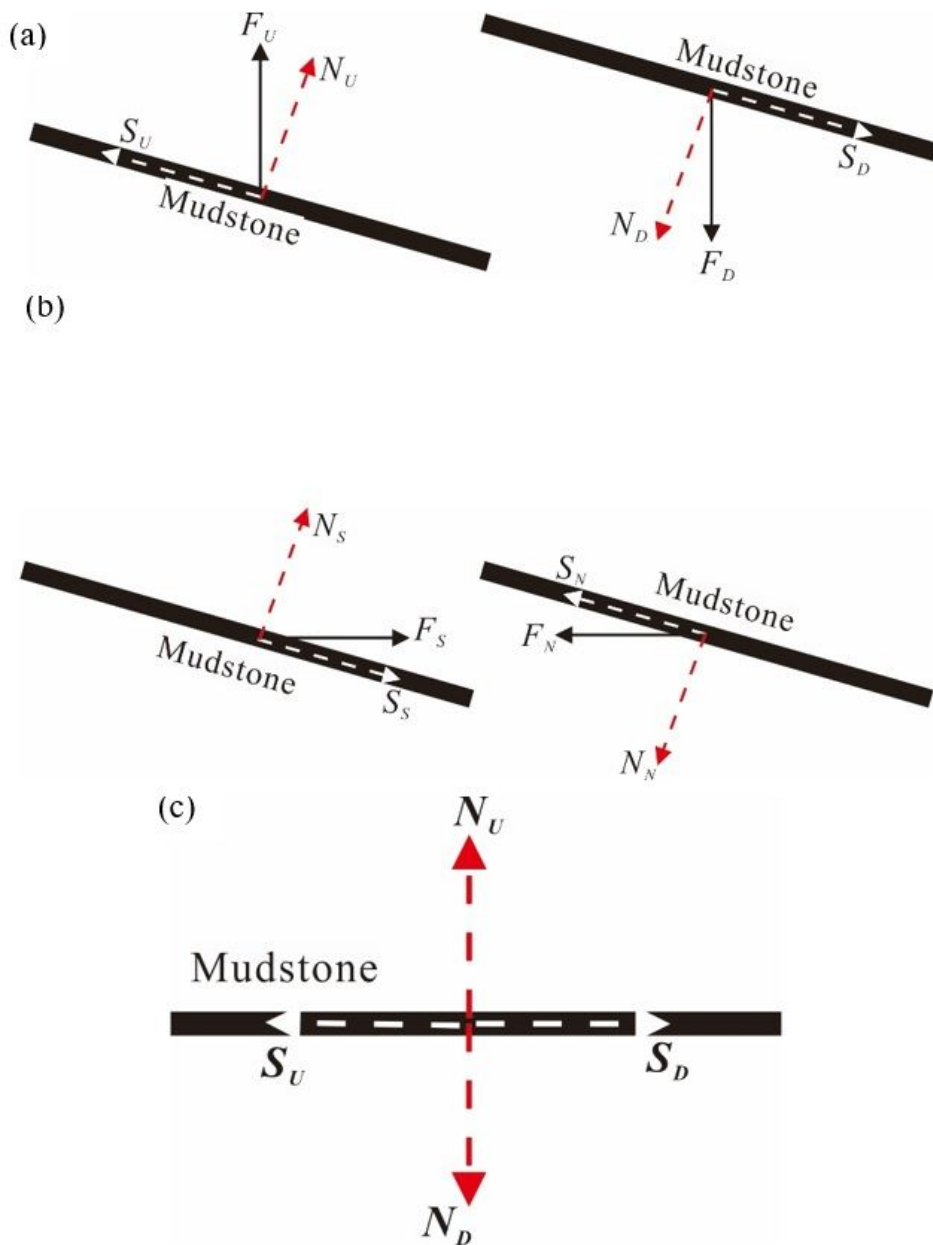


Figure 10

Simplified mechanical mode: (a) decomposition of vertical seismic force, (b) decomposition of horizontal seismic force, and (c) seismic force composition

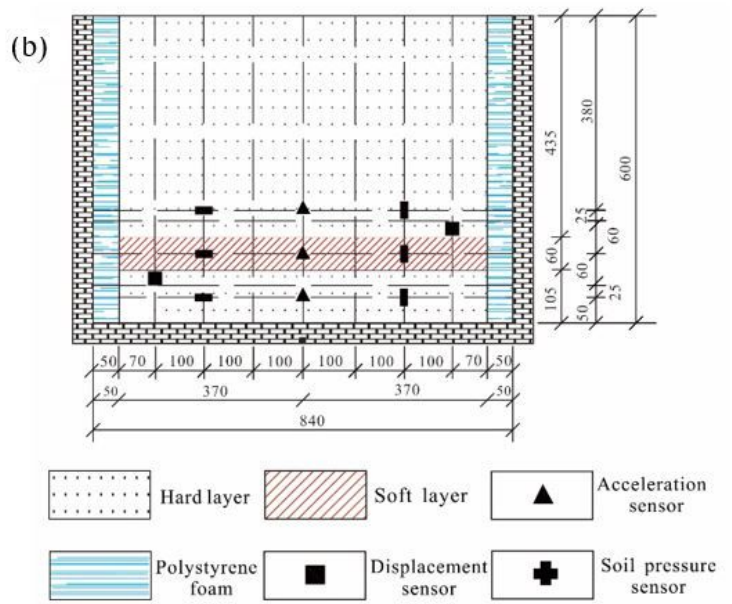
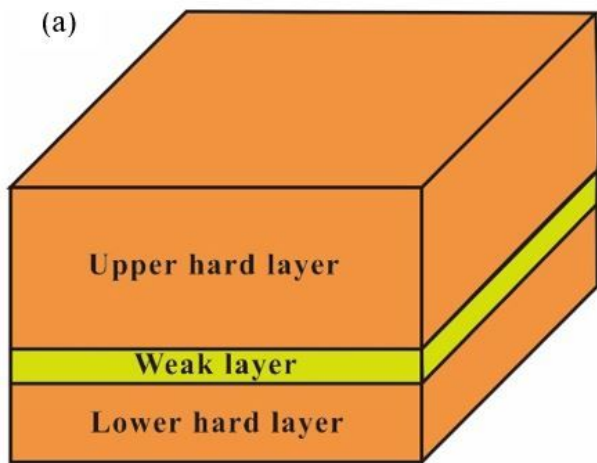
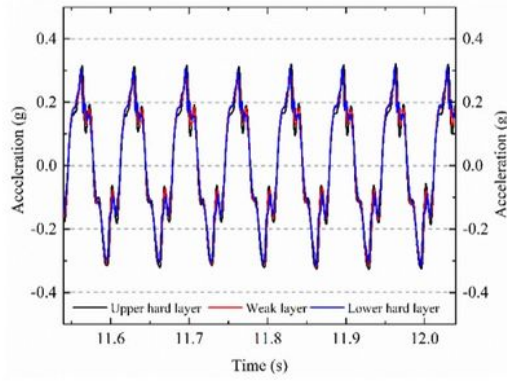
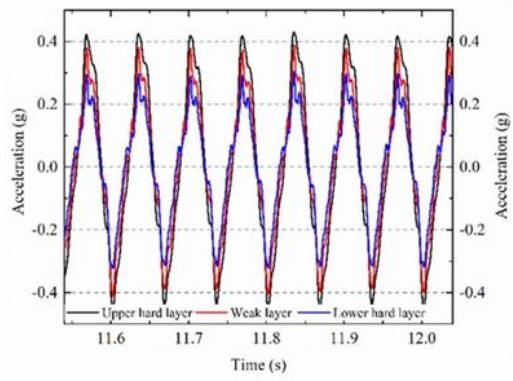


Figure 11

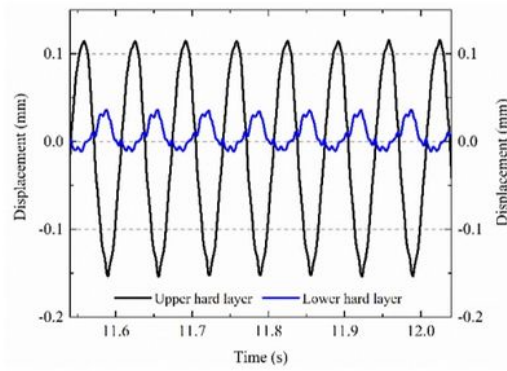
simplified model (a) and a shaking table test model and sensor placement scheme (b)



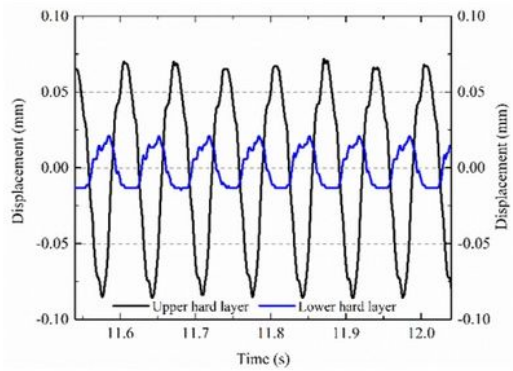
(a) Vertical vibration



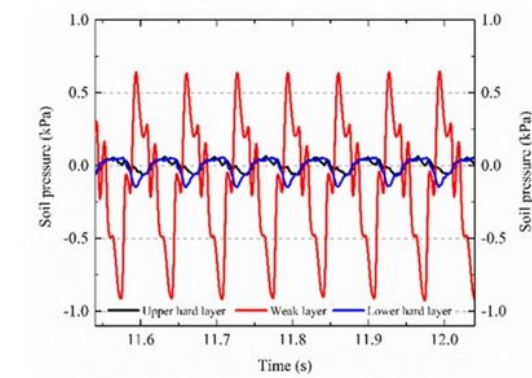
(b) Horizontal vibration



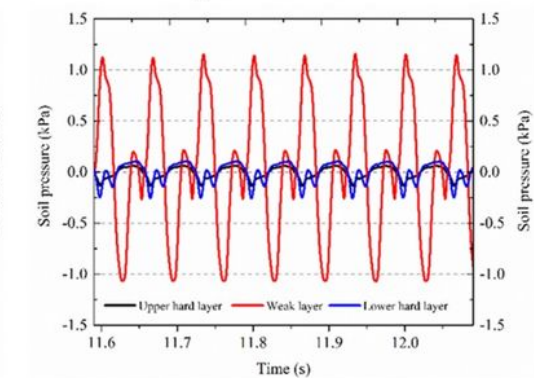
(c) Vertical vibration



(d) Horizontal vibration



(e) Vertical vibration



(f) Horizontal vibration

Figure 12

Shaking table test results

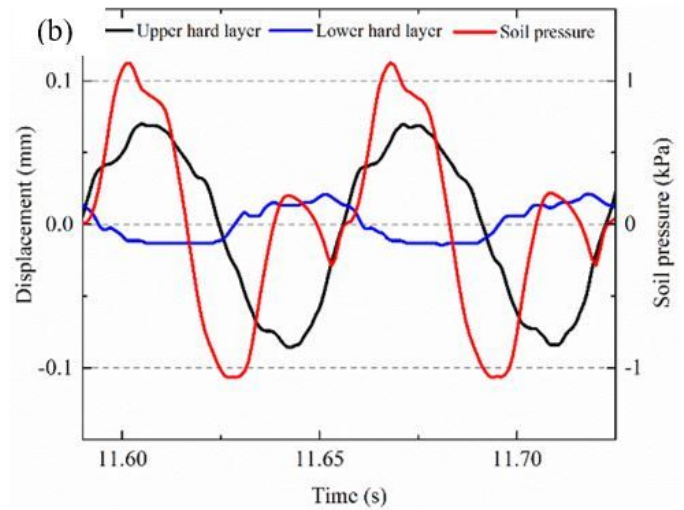
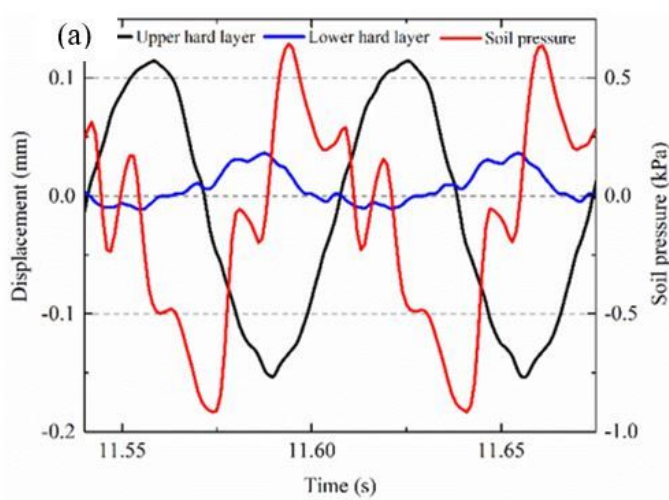


Figure 13

Curves of displacement, soil pressure versus time: (a) vertical vibration, and (b) horizontal vibration

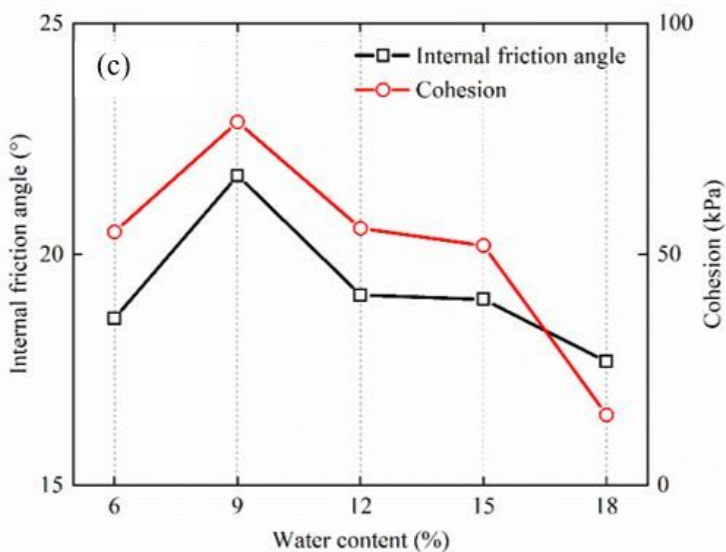
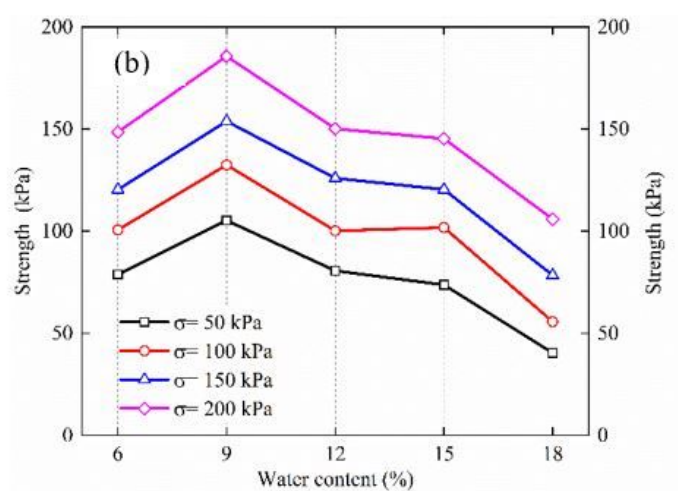
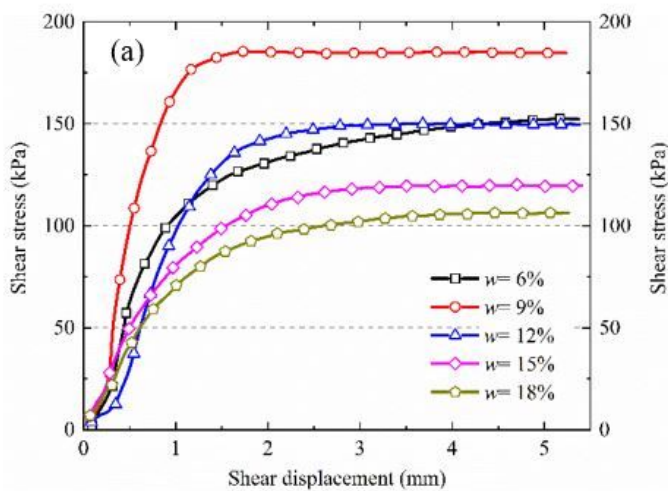


Figure 14

Direct shear test results for samples with different water contents: (a) shear stress versus displacement curves, (b) shear strength versus water content curves, and (c) internal friction angle and cohesion versus water content curves

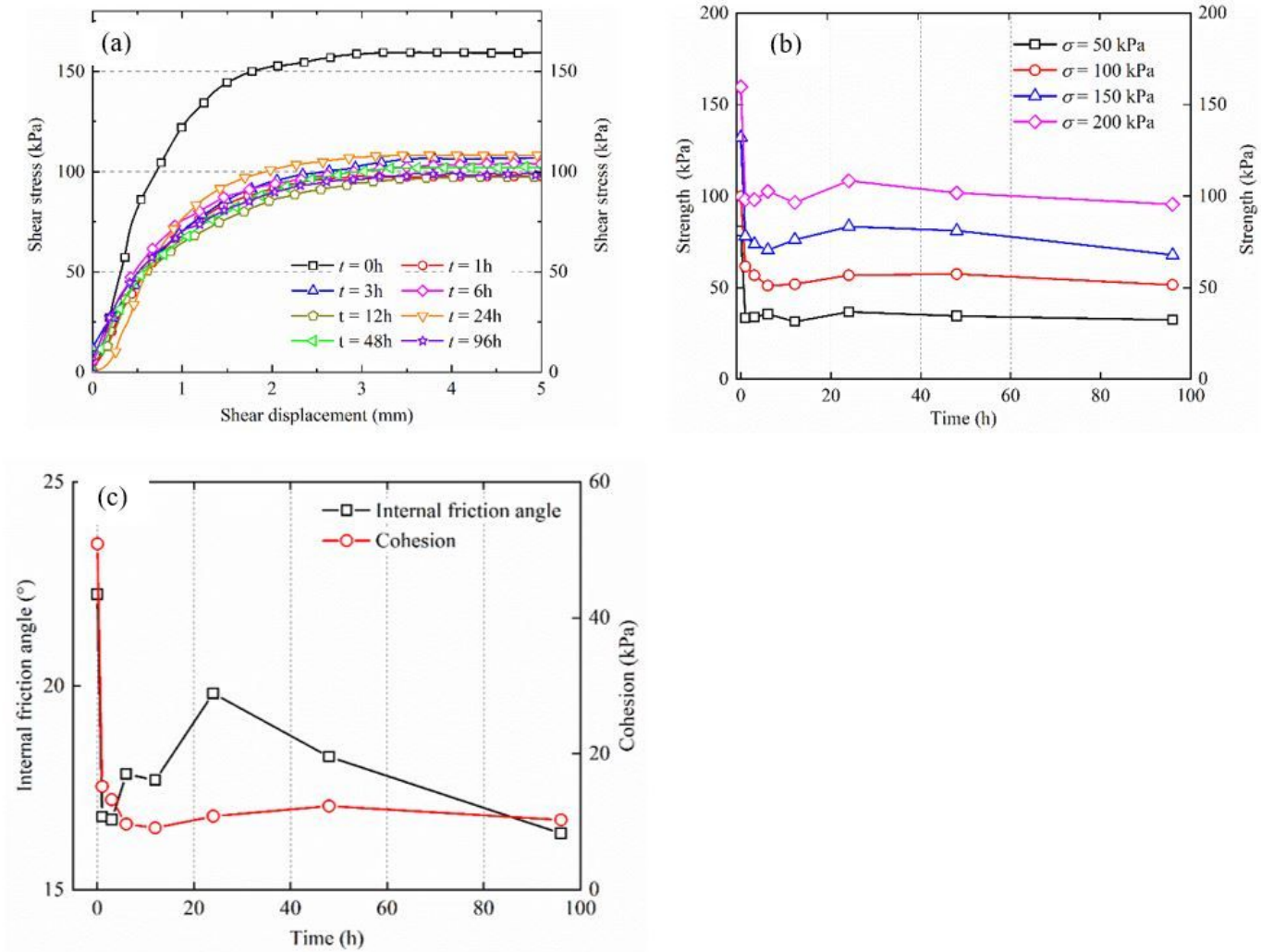


Figure 15

Direct shear test results for samples with different immersion times: (a) shear stress versus displacement curves for $\sigma = 200$ kPa, (b) shear strength versus water immersion time curves, (c) internal friction angle and cohesion versus immersion time curves

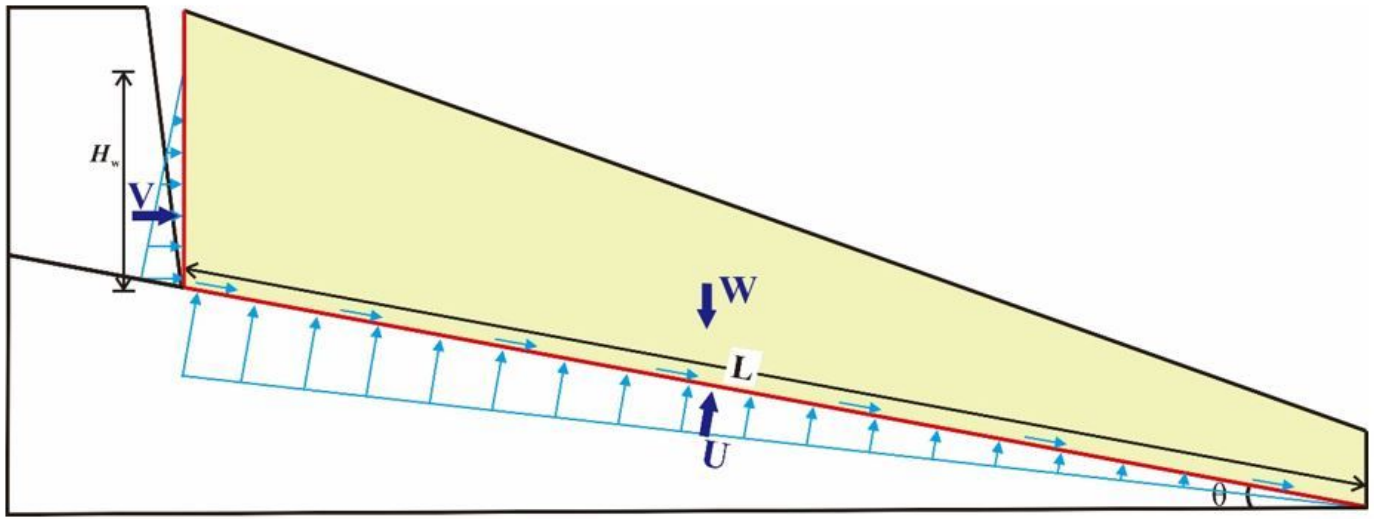


Figure 16

Stability calculation of profile B-B'

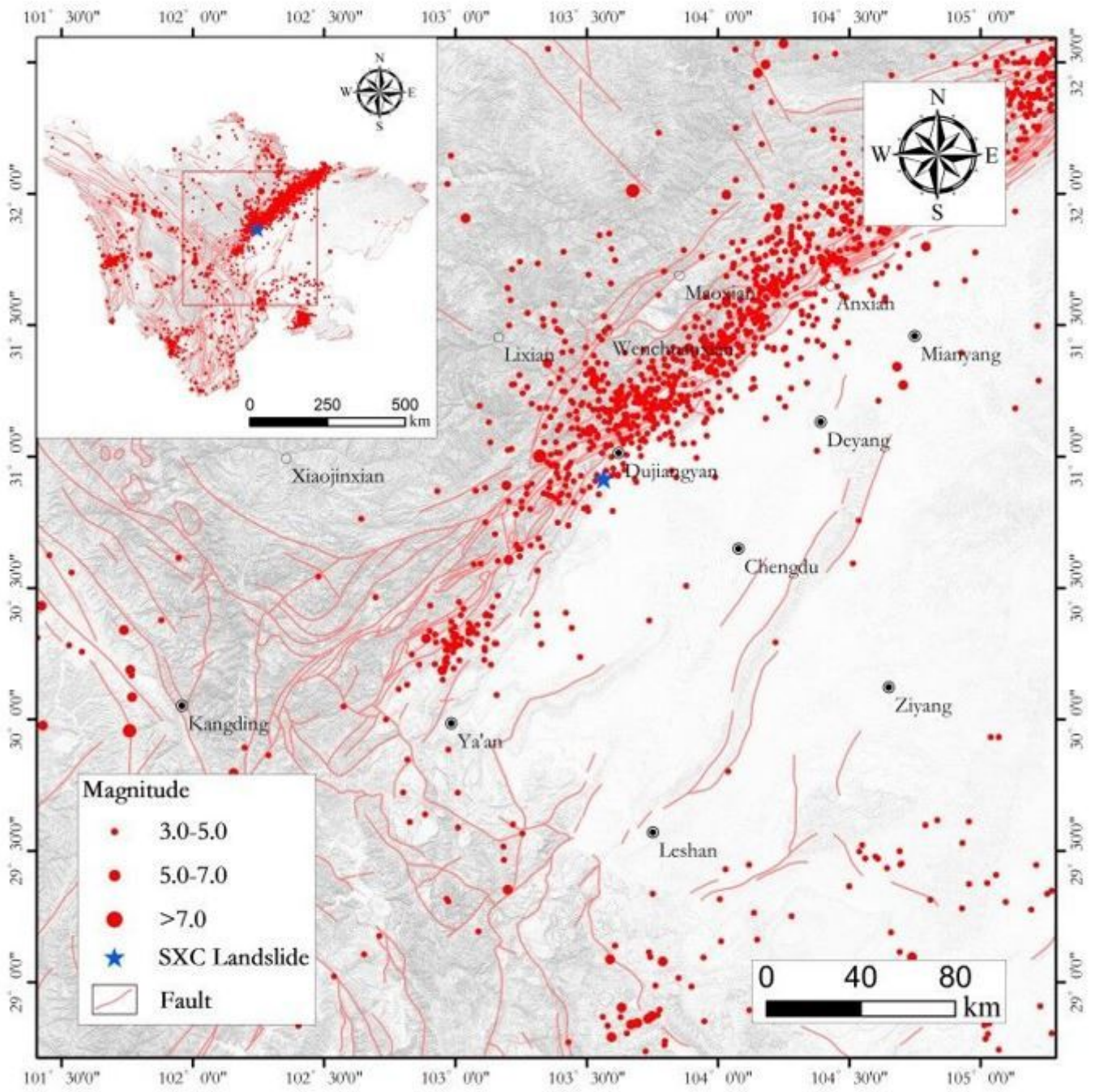


Figure 17

Earthquake events occurring in the adjacent area since 1900 Note: The designations employed and the presentation of the material on this map do not imply the expression of any opinion whatsoever on the part of Research Square concerning the legal status of any country, territory, city or area or of its authorities, or concerning the delimitation of its frontiers or boundaries. This map has been provided by the authors.

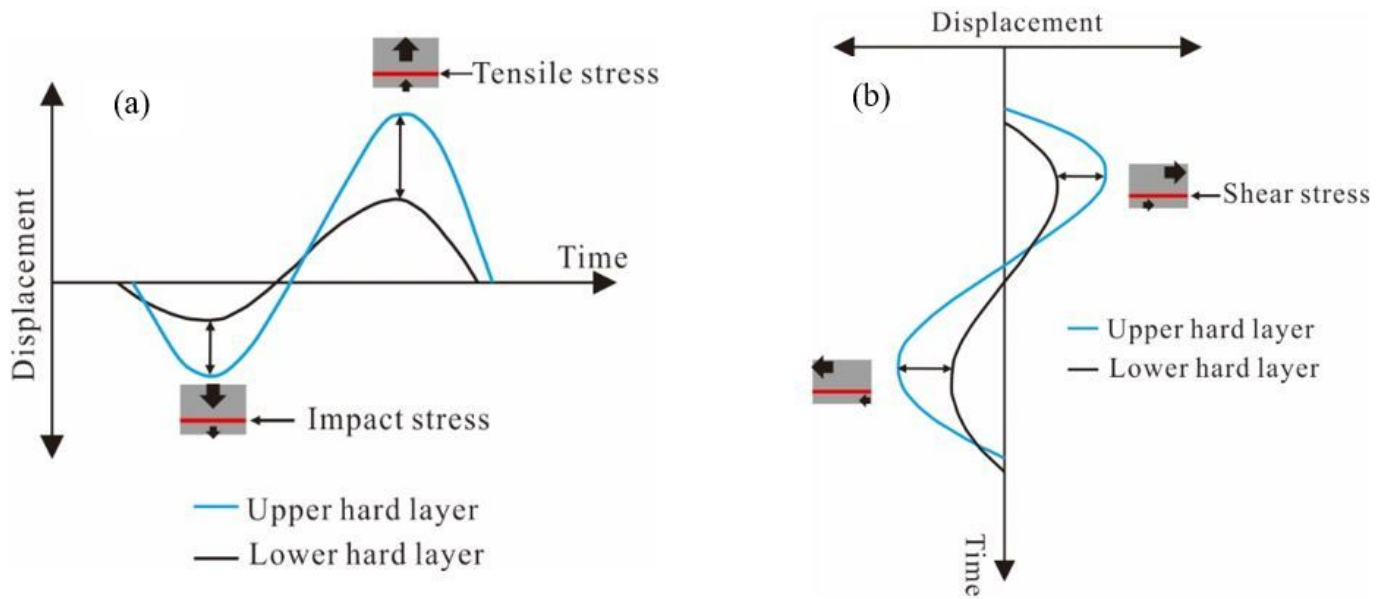


Figure 18

Diagram of incompatible deformation in the model: (a) impact and tension stresses, (b) shear stress

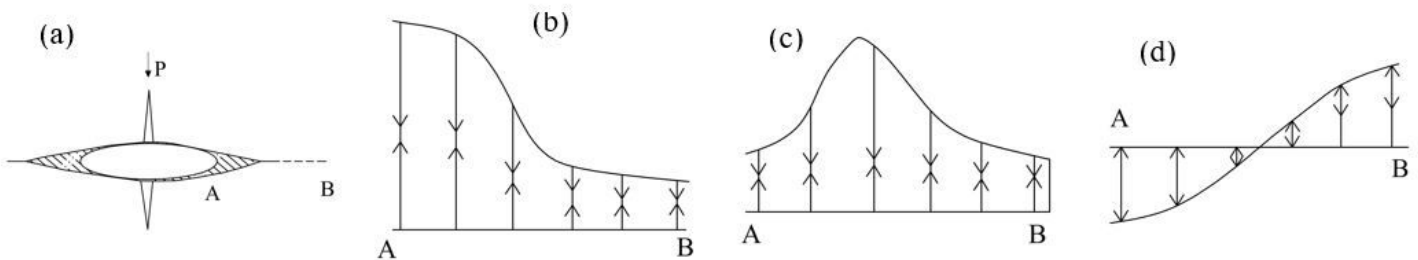


Figure 19

Mechanisms of crack propagation under compression stress (modified by Lajtai 1977): (a) the tension fracture pattern of the original crack, (b) the stress concentration position at the crack tip, (c) transfer of stress concentration position, and (d) residual tension stress

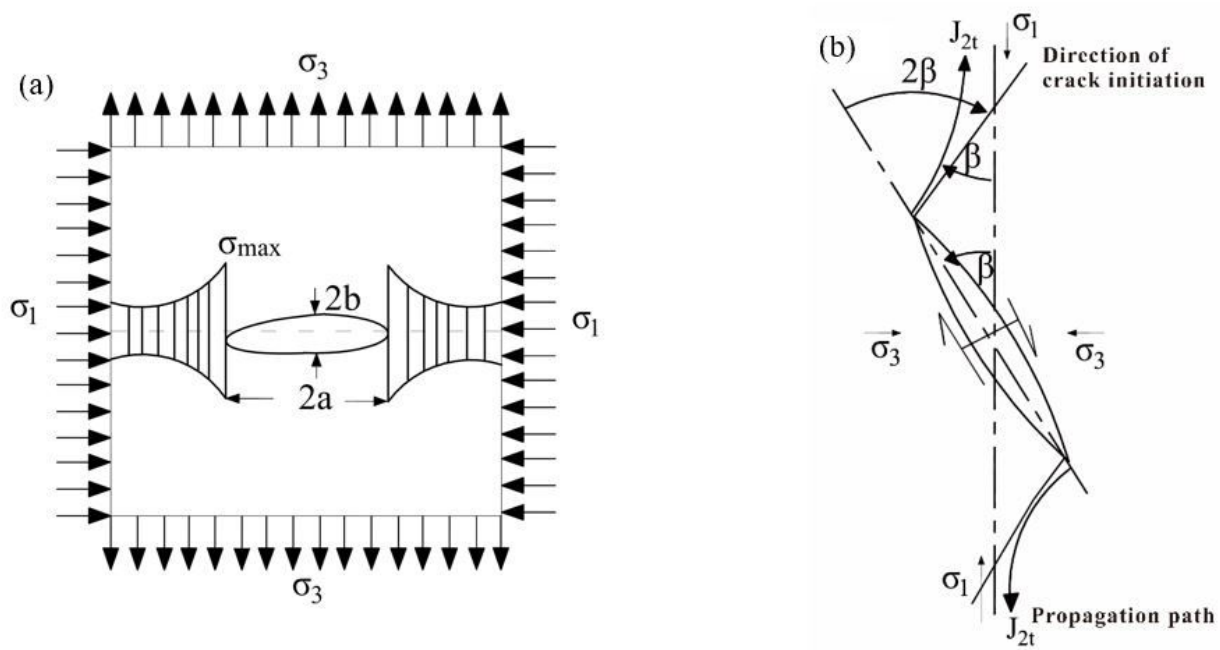


Figure 20

Mechanisms of crack propagation under tension stress (a) and mechanisms of tension failure under compression stress (b)

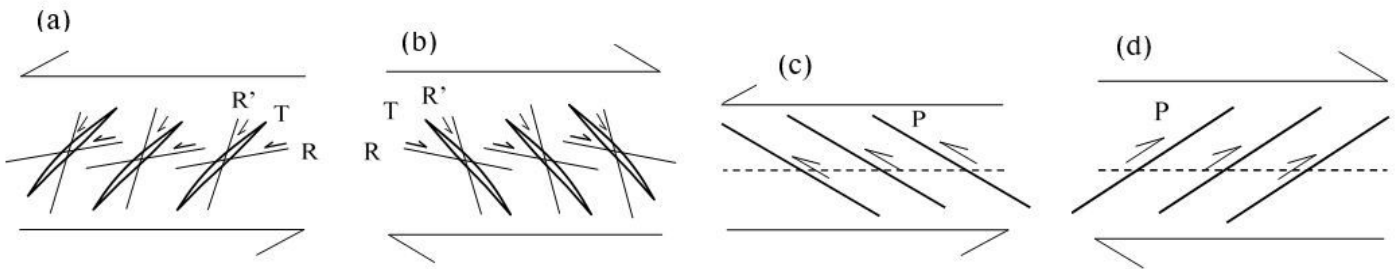


Figure 21

Mechanisms of crack propagation under cyclic shear stress, a. sinistral tension cracks, b. dextral tension cracks, c. sinistral compressive-torsion cracks, d. dextral compressive-torsion cracks

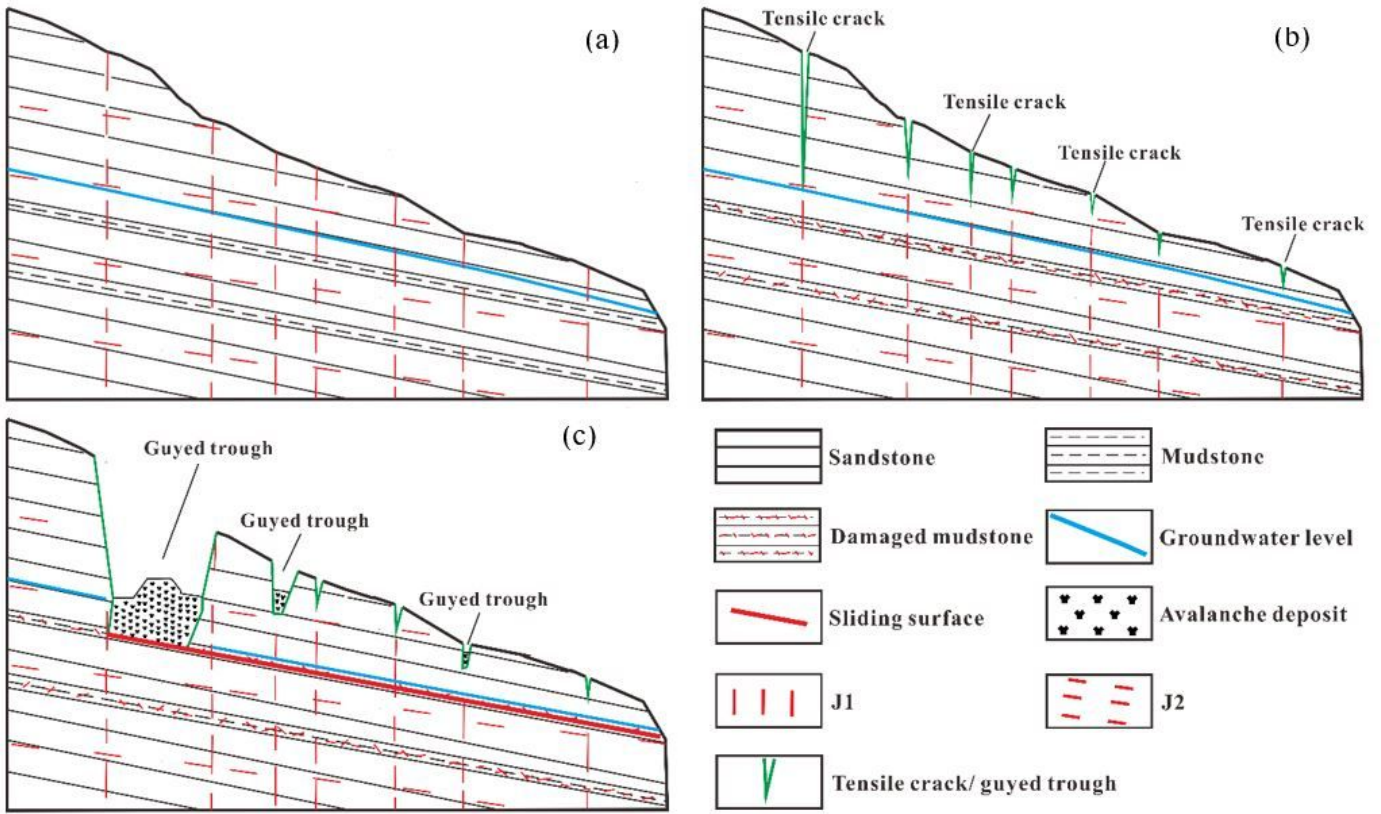


Figure 22

Formation and evolution process of the cracked slope, (a) original slope with joints (b) seismic cracks formed by historical earthquakes, (c) progressive deformation of slope and the formation of tension cracks under the combined influence of earthquake, rainfall and gravity

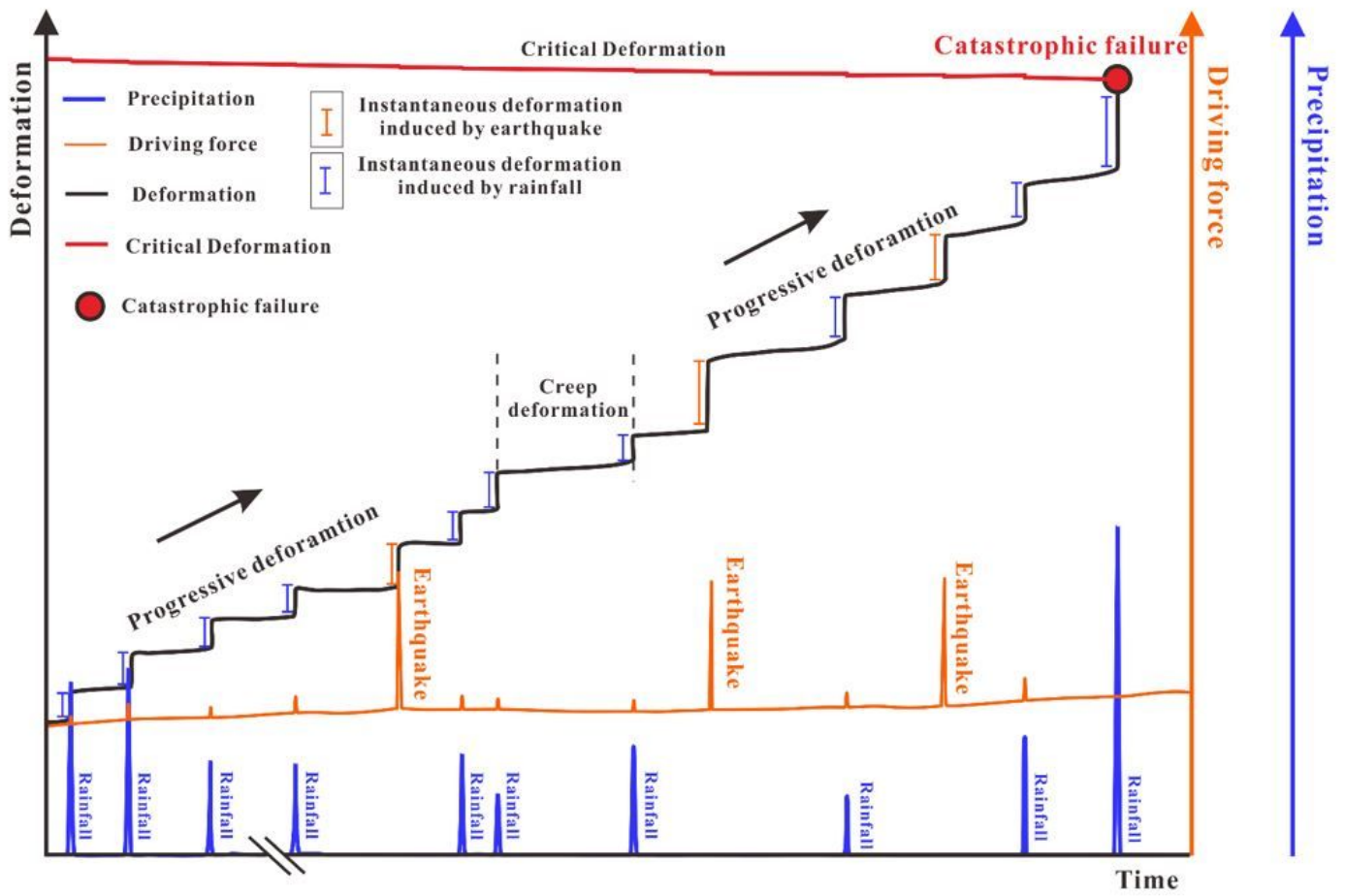


Figure 23

Progressive deformation process of SXC slope under the influence of historical earthquakes, gravity and rainfall

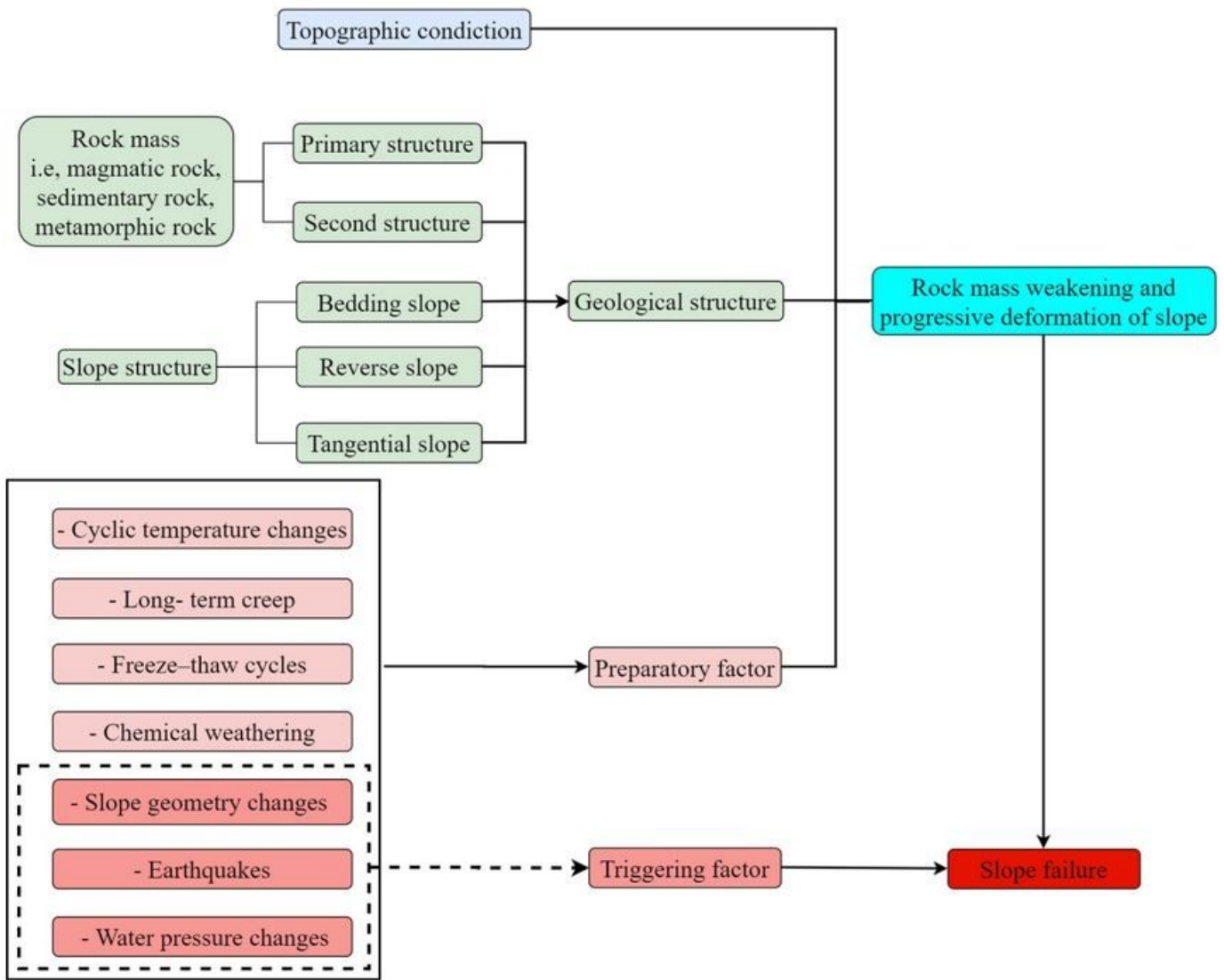


Figure 24

Flowchart illustrating the rock mass weakening and progressive failure of slope